ADA035051

6
NU

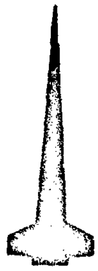

TECHNICAL REPORT RL-76-12

ROCKET EXHAUST FLOW IN TUBE LAUNCHERS

James L. Batson
Ground Equipment and Materials Directorate
US Army Missile Research, Development and Engineering Laboratory
US Army Missile Command
Redstone Arsenal, Alabama 35809

20000726060

19 January 1976

Approved for public release; distribution unlimited.

U.S. ARMY MISSILE COMMAND
Redstone Arsenal, Alabama

**Reproduced From
Best Available Copy**

DDC
RECEIVED
FEB 1 1977
B

ORM AMSMI-1021, 1 DEC 65 PREVIOUS EDITION IS OBSOLETE

DISPOSITION INSTRUCTIONS

DESTROY THIS REPORT WHEN IT IS NO LONGER NEEDED. DO NOT RETURN IT TO THE ORIGINATOR.

DISCLAIMER

THE FINDINGS IN THIS REPORT ARE NOT TO BE CONSTRUED AS AN OFFICIAL DEPARTMENT OF THE ARMY POSITION UNLESS SO DESIGNATED BY OTHER AUTHORIZED DOCUMENTS.

TRADE NAMES

USE OF TRADE NAMES OR MANUFACTURERS IN THIS REPORT DOES NOT CONSTITUTE AN OFFICIAL INDORSEMENT OR APPROVAL OF THE USE OF SUCH COMMERCIAL HARDWARE OR SOFTWARE.

UNCLASSIFIED

SECURITY CLASSIFICATION OF THIS PAGE (When Data Entered)

REPORT DOCUMENTATION PAGE

READ INSTRUCTIONS BEFORE COMPLETING FORM

(14)

1. REPORT NUMBER: RL-76-12

2. GOVT ACCESSION NO.

3. RECIPIENT'S CATALOG NUMBER

(6)

4. TITLE (and Subtitle): ROCKET EXHAUST FLOW IN TUBE LAUNCHERS.

(9)

5. TYPE OF REPORT & PERIOD COVERED: Technical rept.

6. PERFORMING ORG. REPORT NUMBER

(10)

7. AUTHOR(s): James L. Batson

8. CONTRACT OR GRANT NUMBER(s)

(16)

9. PERFORMING ORGANIZATION NAME AND ADDRESS

Commander
US Army Missile Command
Attn: DRSMI-RL
Redstone Arsenal, Alabama 35809

10. PROGRAM ELEMENT, PROJECT, TASK AREA & WORK UNIT NUMBERS

(DA) 1M362303A214
AMCMSC 632303.11.21405.60

11. CONTROLLING OFFICE NAME AND ADDRESS

Commander
US Army Missile Command
Attn: DRSMI-RPR
Redstone Arsenal, Alabama 35809

(11)

12. REPORT DATE: 19 January 1976

13. NUMBER OF PAGES: 106

14. MONITORING AGENCY NAME & ADDRESS (if different from Controlling Office)

(12) 13p.

15. SECURITY CLASS. (of this report): UNCLASSIFIED

15a. DECLASSIFICATION/DOWNGRADING SCHEDULE

16. DISTRIBUTION STATEMENT (of this Report)

Approved for public release; distribution unlimited.

17. DISTRIBUTION STATEMENT (of the abstract entered in Block 20, if different from Report)

18. SUPPLEMENTARY NOTES

19. KEY WORDS (Continue on reverse side if necessary and identify by block number)

Free flight rocket technology
Rocket exhaust
Tube launchers
Method of characteristics
Flow field

20. ABSTRACT (Continue on reverse side if necessary and identify by block number)

The present investigation, which was primarily of an experimental nature, was undertaken to define the flow field produced when an underexpanded jet is exhausted from a conical nozzle (rocket exhaust) into a cylindrical tube (tube launcher). The experimental data included the reservoir conditions for the nozzle, the static pressure distribution along the cylinder wall, pitot probe surveys at the cylinder exit, and photographs of the flow exhausting from the tube. Of principal concern were the effects on the flow field of tube length, of reservoir conditions, and of test time. Although room-temperature nitrogen

→ over

DD FORM 1 JAN 73 1473 EDITION OF 1 NOV 65 IS OBSOLETE

UNCLASSIFIED

SECURITY CLASSIFICATION OF THIS PAGE (When Data Entered)

400 406

4/B

Block 20 (Concluded)

was used as the test gas in most of the tests, several tests used actual rockets statically fired into the same cylindrical tubes. The experimentally determined flow field characteristics were compared with the experimental data of others, with a method of characteristics analysis developed for the present investigation, and with the flow field model of Fabri and Siestrunck.

TABLE OF CONTENTS

CHAPTER PAGE

I INTRODUCTION 5

II LITERATURE REVIEW 8

III ANALYTICAL INVESTIGATION 15

IV EXPERIMENTAL INVESTIGATION 25

V RESULTS AND DISCUSSION 51

VI CONCLUDING REMARKS 83

APPENDIX A
FINITE DIFFERENCE EQUATIONS FOR STEADY, AXISYMMETRIC, POTENTIAL FLOW AND STEADY, AXISYMMETRIC, ROTATIONAL FLOW 85

APPENDIX B
DETAILED COMPUTATION METHOD FOR AXIALLY SYMMETRIC ROTATIONAL FLOW REGION BY AN APPROXIMATE FINITE DIFFERENCE METHOD OF CHARACTERISTICS 91

APPENDIX C
FLOW CHARACTERISTICS 101

LIST OF REFERENCES 111

DEFINITION OF SYMBOLS

Symbol	Definition
A	Area of spherical surface
D	Internal diameter of tube
M	Mach number
m	Number of increments or iterations
P	Pressure
R	Spherical radius
r, ϕ, z	Cylindrical coordinates
S	Entropy
T	Temperature
β	Angle of the impingement shock with respect to the tube axis
γ	Ratio of specific heats
$\Delta\theta$	An increment of the nozzle half angle
θ	Angle of the flow with respect to the tube axis
θ_n	Conical nozzle half angle
μ	Mach angle
ν	Prandtl-Meyer angle
Superscript	
$*$	Evaluated at the nozzle throat
Subscript	
a	Evaluated at atmospheric conditions
b	Evaluated in the dead air region

DEFINITION OF SYMBOLS (Concluded)

o	Evaluated at stagnation conditions
p	Evaluated at point p
t	Evaluated at the tube wall
w	Evaluated along the tube wall

ACCESSION for
NTIS White Section ☑
DDC Buff Section ☐
UNANNOUNCED ☐
JUSTIFICATION ....
BY ....
DISTRIBUTION/AVAILABILITY CODES
Dist. AVAIL. and/or SPECIAL
A

CHAPTER I

INTRODUCTION

A primary problem associated with the structural design of lightweight cylindrical tube rocket launchers is the prediction of the maximum pressures or forces exerted on the tube wall by the flow exhausting from the rocket nozzle. An understanding of the rocket exhaust flow field in the launcher is a prerequisite to the determination of the pressure distribution along the tube wall and to the optimum launcher structural design. The current demand for more powerful rockets coupled with the requirement for lightweight launchers has only recently emphasized the need for a knowledge of the flow field inside the launcher. Up to now, the maximum pressure in the tube was assumed to be that at the nozzle exit.* The structural integrity of launcher was usually demonstrated by firing the rocket from the launcher. Some experimental information was obtained. However, it was not used to gain an understanding of the exhaust flow but to ascertain if the launcher could withstand the pressures. Therefore, the research reported in this paper has been directed to the understanding of the rocket exhaust flow in the launcher or, in other words, of an axisymmetric, underexpanded jet exhausting into a cylindrical tube.

A literature survey which was conducted through NASA's Scientific and Technical Information Facility and the Defense Documentation Center failed to provide specific information regarding

---

* US Army Missile Command Report No. RL-TR-71-9, dated 30 July 1971.

PRECEDING PAGE BLANK-NOT FILMED

the rocket exhaust field within a cylindrical tube launcher. However, information pertaining to other applications was found which was applied to this specific application. A flow model based upon the findings of the literature search was devised to theoretically approximate the flow within the tube. A computer program which utilized the method of characteristics for steady, axisymmetric, rotational flow and which was formulated from that flow model was developed to obtain the pressure distribution along the tube wall and to gain an insight into the characteristics of the flow. For conditions behind the first shock, an approximation method was incorporated into the program to eliminate the necessity of determining the entropy variation in the normal direction along each streamline. The base pressure obtained from experiments and from an existing theoretical method based upon Korst's flow model was used as an input into the computer program.

The theoretical investigation was performed to augment the experimental investigation which constituted the major portion of this research. The experimental investigation consisted primarily of tests employing cold gas flows, although some tests employing hot gas flows were performed. A cold gas facility using dry nitrogen was designed and fabricated to develop a supersonic underexpanded jet. Double base solid propellant* rocket motors produced similar jets for the hot gas tests. These jets were exhausted into instrumented tubes of different lengths to simulate the various positions of the rocket in the launcher during launch. High frequency response pressure transducers were used to sense static wall pressures along the tubes and to obtain pitot pressures within the cold gas flows. High speed pictures were taken of the flow exiting from the tube to aid in the analysis of the flow within the tube.

---

* A double base solid propellant is composed mainly of a colloid of nitroglycerin and nitrocellulose.

Finally, the results from the present experimental investigation and from similar investigations available in the literature are correlated with the results of the theoretical investigation.

CHAPTER II

LITERATURE REVIEW

In 1940, Nusselt [1] conducted experiments with supersonic gas (air) discharging into an enlarged circular cross-section tube. When there is an abrupt increase in flow cross-sectional area as shown in Figure 1, an isolated subsonic region (dead air region) will be created at the corner. If viscous effects are neglected, the pressure in this region, P_b (referred to as base pressure by Wicks [2] is impressed upon the jet boundary and is, in fact, the jet boundary pressure. In reality, the conditions in the dead air region are determined primarily by viscous effects along the jet boundary. Nusselt concluded that the base pressure could be equal to, less than, or greater than the nozzle exit pressure, P_e, depending on the flow

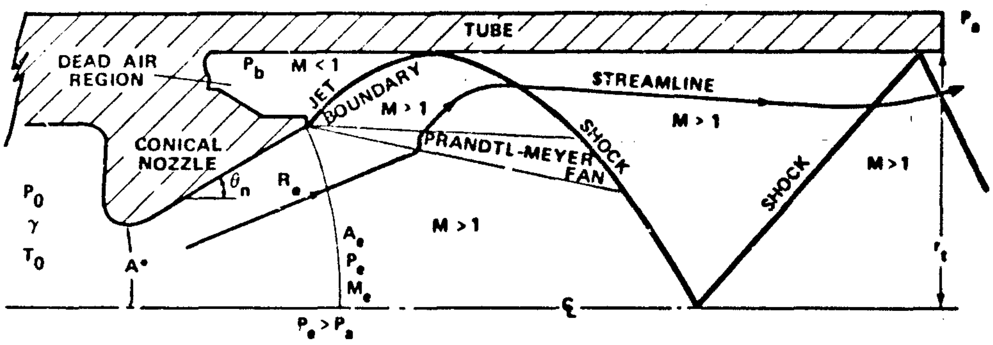
TUBE
P_a
DEAD AIR REGION
P_b
M < 1
JET BOUNDARY
M > 1
STREAMLINE
M > 1
CONICAL NOZZLE
θ_n
R_e
PRANDTL-MEYER FAN
SHOCK
SHOCK
M>1
P_0
γ
T_0
A*
A_e
P_e
M_e
M >1
r_t
℄
$P_e > P_a$

Figure 1. Flow Field for an Axisymmetric, Underexpanded, Supersonic Jet Exhausting into a Cylindrical Tube

total pressure. The description of the flow fields for which these conditions exist was not given.

In 1955, Fabri and Siestrunck [3] published a comprehensive study of a supersonic stream entering an abrupt circular enlargement. The type of flow within the enlarged section or tube varied with an increase in total pressure from mixed flow (subsonic and supersonic in the tube) with flow separation in the nozzle to fully developed supersonic flow throughout the tube. As did Nusselt, they used the base pressures and total pressures to define the flows and, by the use of shadowgraphs, were able to associate these pressures with visual observations of the flow fields. Shadowgraphs obtained by Fabri and Siestrunck [3] of the flow field with the nozzle exhaust filling the tube are reproduced in Figure 2. A complete sequence

INITIAL TRANSITION FLOW PATTERN

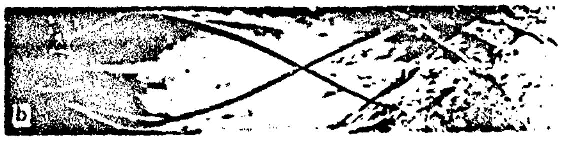

INTERMEDIATE TRANSITION FLOW PATTERN

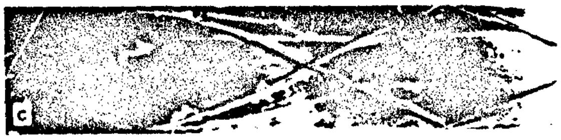

FULLY DEVELOPED SUPERSONIC FLOW PATTERN

Figure 2. Shadowgraphs of Tube Flows with Nozzle Exhaust Filling the Tube [3]

of the flows are shown in references [3], [4], and [5]. The base pressure/total pressure relation corresponding to the shadowgraphs is shown in Figure 3. Figure 3 shows that the base pressure decreases as the total pressure increases in the mixed flow regime and increases as the total pressure increases in the supersonic regime.

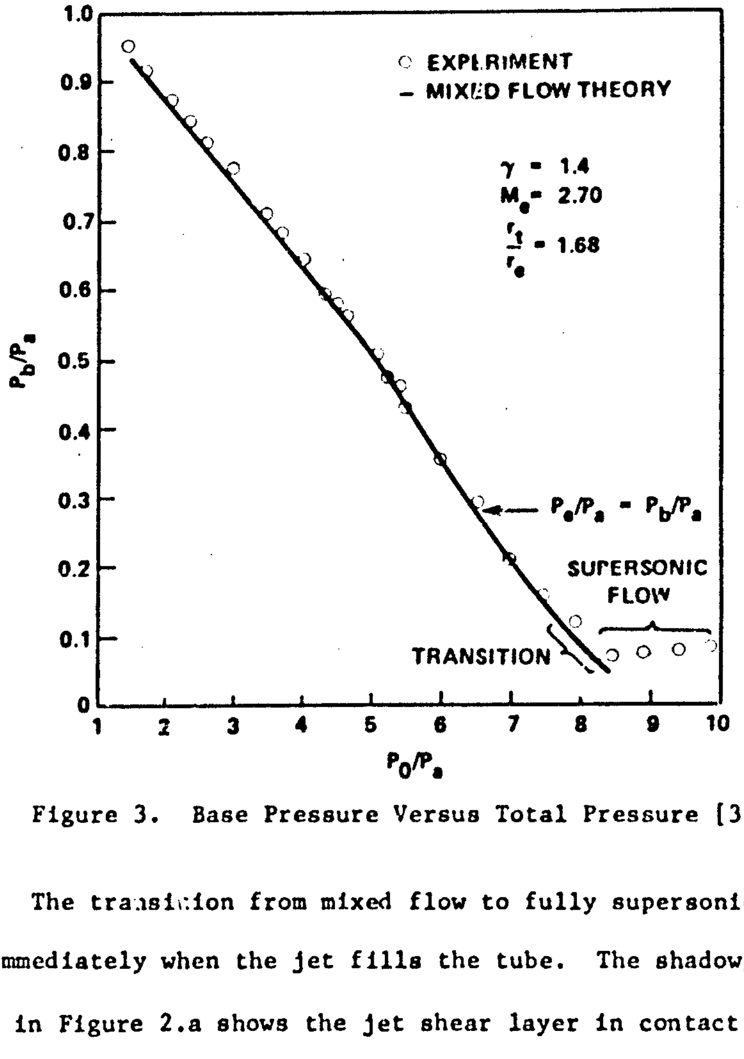

Figure 3. Base Pressure Versus Total Pressure [3]

The transition from mixed flow to fully supersonic flow begins immediately when the jet fills the tube. The shadowgraph pictured in Figure 2.a shows the jet shear layer in contact with the wall. A series of lambda shocks form in the tube reducing the supersonic flow to subsonic. The subsonic shear layer along the tube wall provides a relatively large means of communication for the downstream conditions back to the dead air region. The corresponding transition base pressure is indicated in Figure 3. Transition begins at a base pressure which is lower than the nozzle exit pressure indicating that the nozzle exhaust flow is expanding from the nozzle exit diameter toward the larger tube diameter.

An increase in total pressure causes the base pressure to decrease. The gases in the jet boundary expand and impact the wall. An oblique shock wave forms (Figure 2.b), but the shock pattern breaks down, indicating that supersonic flow does not exist throughout the tube. Once the total pressure is sufficiently increased, the flow in the tube is supersonic and intersecting oblique shock patterns form throughout the tube (Figure 2.c). Note that the upstream flow characteristics in the supersonic flow should now become essentially independent of downstream conditions. Crocco [5] noted:

> Observe that, as the pictures (refer to Figure 2) show clearly, the shocks do not reach the wall because of the presence of subsonic flows in the boundary layer and in the zone where the jet mixes with the gases recirculating in the dead water (air) region. However, these subsonic regions are thin, and if their longitudinal extent is sufficient, they cannot prevent the isolation of the dead water region from the downstream effects.

The comparison of theory with experimental data presented in Figure 3 indicates that the one-dimensional mixed flow theory of Fabri and Siestrunck is adequate for the mixed flow regime. However, one-dimensional theory no longer applies with the advent of a complicated axisymmetric supersonic flow. Also, the onset of supersonic flow cannot be predicted with one-dimensional theory. According to Fabri and Siestrunck, the base pressure/total pressure relation for fully developed supersonic flow is $P_b/P_0 =$ constant. The value of this constant must be obtained either from experiment or from a theory which involves the consideration of the shear layers bounding the dead air region along with the characteristics of the supersonic flow.

Fabri and Siestrunck recorded the tube wall pressures and presented the ratio P_w/P_b as a function of tube length for the supersonic regime (Figure 4). The results of their axisymmetric method of characteristics study are also shown in Figure 4. The characteristics net, which is not presented, was shown as a mirror image of a shadowgraph similar to Figure 2.c and included the shock emanating from the jet boundary-wall intersection and its reflection from the centerline back to the wall. No information was provided regarding the details of solution of the complex axisymmetric, rotational flow with multiple shocks.

An interesting practical application of the type of flow being investigated is found in wind tunnels with a free jet test section. The particular application was treated theoretically (one-dimensional theory) by Hermann [6]. As can be noted from later publications of Fabri and Siestrunck [4, 7], another associated practical application is the supersonic ejector. In 1958, Goethert [8] proposed that an ejector which utilized the test engine exhaust (rocket nozzle exhaust) could be used to provide high altitude simulation pressures in a test cell. This triggered a flurry of activity by the

U.S. Air Force at Arnold Air Force Station, Tennessee, and Edwards Air Force Base, California [9 - 18].

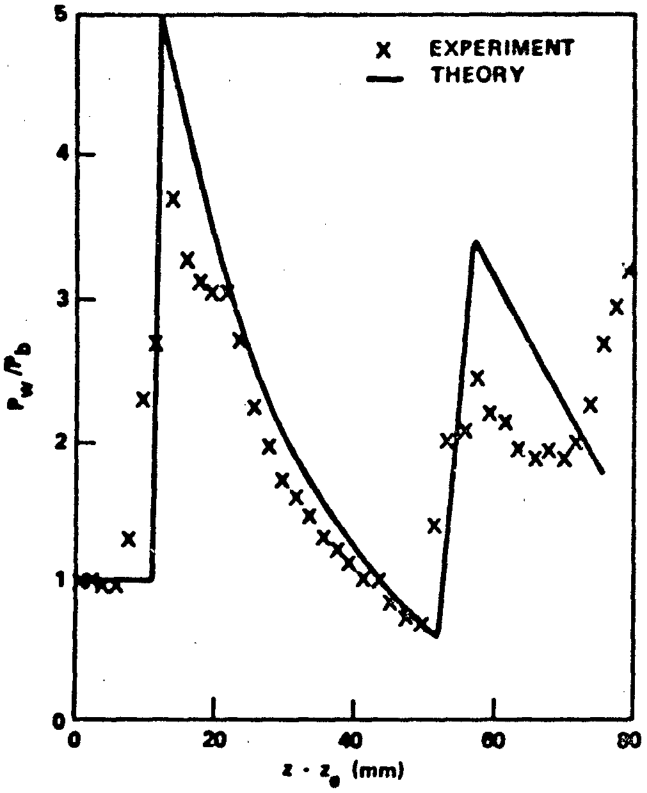

Figure 4. P_w/P_b Versus Tube Length for Fully Developed Supersonic Flow [3]

The ejector-diffuser application is based upon the relatively low base pressure obtained when exhausting a supersonic stream into an enlarged section. The minimum base pressure occurs at the beginning of the supersonic regime (Figure 3). Most of the work in this field has revolved around understanding the base pressure phenomenon in order to obtain the minimum base pressure possible. Consequently, the characterization of the supersonic tube flow has been neglected, especially at higher total pressures than those necessary to produce minimum base pressure.

The adaptation of Korst's base pressure flow model [19] to axisymmetric ejectors without induced flow by Bauer [16, 17] has evolved as the best method of predicting base pressure. This base pressure prediction method is also applicable to the specific problem posed in this work. Other pertinent theories, i.e., those of Crocco and Lees [20], Zumwalt [21], Nash [21], Greenwood [22], and Lamb [23] may be adaptable to this specific problem. Bauer [17] and German et al. [18], proposed a method for the determination of the tube wall pressure at the jet boundary-wall intersection. This pressure, termed by Bauer as the peak recompression static pressure, is also based on Korst's theory. This prediction method agreed favorably with their experimental data.

CHAPTER III

ANALYTICAL INVESTIGATION

Flow Model

A highly underexpanded supersonic, short duration jet exhausting from a conical nozzle into a short tube with an inside diameter slightly larger than the nozzle exit characterizes the flowfield of tube launched, folding fin rockets. A simple flow model has been devised to describe such a flow. The model is based upon the fully developed supersonic flow as defined by Fabri and Siestrunck.

The operating rocket motor chamber pressures vary according to the burning characteristics of the grain. The maximum pressures range from 250 to 350 (P_0/P_a), depending on the rocket. As can be noted from Figure 3, these total pressures are far in excess of that required to produce supersonic flow. Foster [11] experimentally investigated flows with maximum $P_0/P_a = 70$. The large total pressures coupled with the geometry should produce fully developed supersonic flow.

In the present model steady flow is assumed. However, in reality, the flow is not steady during rocket motor ignition or chamber pressure tailoff. Therefore, the analysis will concentrate on those data obtained during the quasi-steady flow which exists during the interval when the stagnation pressure is at or near a maximum. The flow field during this time interval is of interest from an engineering standpoint, because the stresses in the tube wall are at a maximum. Heat transfer and real gas effects (including possible chemical reactions in the tube) are neglected. However, they should be included if a more rigorous analysis of the hot gas flow is desired. The flow is assumed to be inviscid, although a theory which includes the viscous nature of the gas at the jet boundary is used to predict base pressures Figure 5 is a schematic of the flow model.

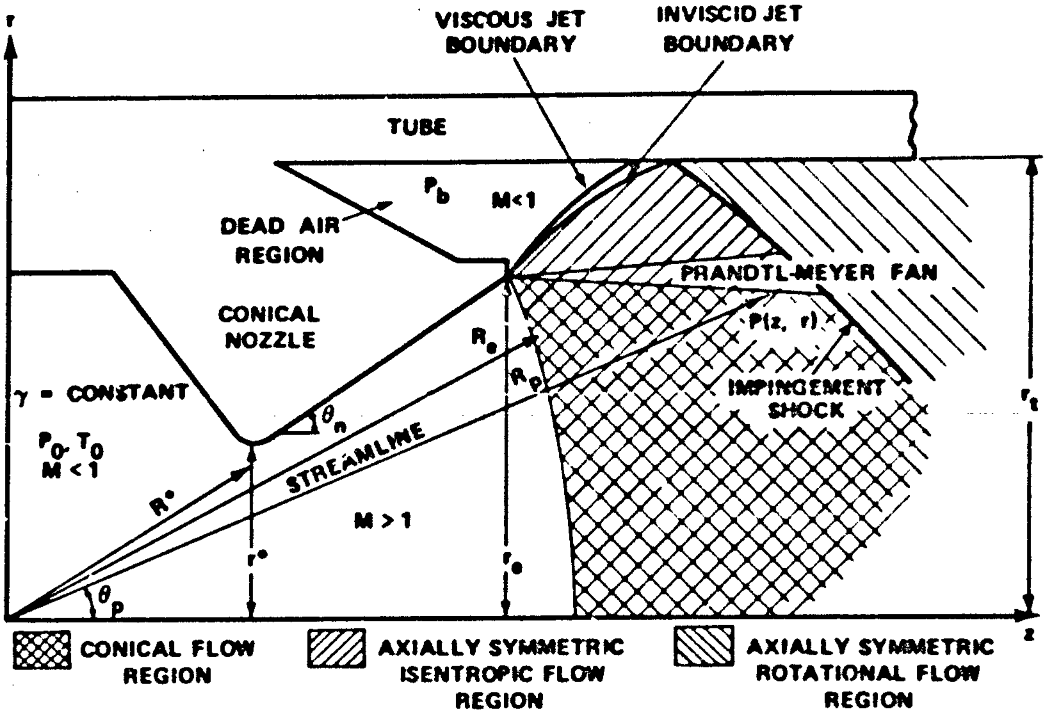
r
VISCOUS JET BOUNDARY
INVISCID JET BOUNDARY
TUBE
P_b
M<1
DEAD AIR REGION
CONICAL NOZZLE
PRANDTL-MEYER FAN
P(z, r)
R_e
R_p
IMPINGEMENT SHOCK
r_t
γ = CONSTANT
θ_n
P_0, T_0
M < 1
STREAMLINE
R^*
M > 1
r^*
r_e
θ_p
z
CONICAL FLOW REGION
AXIALLY SYMMETRIC ISENTROPIC FLOW REGION
AXIALLY SYMMETRIC ROTATIONAL FLOW REGION

Figure 5. Flow Model for Axisymmetric, Underexpanded, Supersonic Jet Exhausting into a Cylindrical Tube

The radial flow region bounded by the nozzle exit spherical radius, R_e, Prandtl-Meyer expansion fan, and impingement shock is termed the conical flow region. The characteristics of the flow in this region are determined from geometry and the stream tube relation,

$$\frac{R_p}{R^*} = f(\gamma, M_p) \quad . \tag{1}$$

The axially symmetric, isentropic flow region is bounded by the Prandtl-Meyer expansion fan, inviscid jet boundary, and impingement shock. In actuality, this region may not be isentropic as assumed. The expansion waves generated by the expansion of the gas from the nozzle exit pressure to the base pressure reflect from the jet boundary as compression waves. These waves will coalesce to form a boundary shock at some finite distance downstream of the nozzle. However, if the impingement shock intervenes before a strong boundary shock can develop, the isentropic assumption should be valid. This was found to be valid for the cases considered in the theoretical investigation.

Once the jet boundary intersects the tube wall, an impingement shock develops as a result of the turning of the gases along the wall. The flow aft of the impingement shock (the axially symmetric, rotational flow region) is highly rotational and must be treated as nonisentropic. From the launcher design viewpoint, this is the most important region because maximum wall pressure exists behind the impingement shock.

Governing Equations

The flow model is amenable to existing analytical techniques which must be solved by numerical methods. Three separate analyses, one for each region, are used. The conical flow region, the simplest to analyze, is governed by the isentropic relations and geometry with regard to the stream tube relation:

$$\left[\frac{R^*}{R_p}\right]^2 = \left[\frac{\gamma + 1}{2}\right]^{\frac{\gamma + 1}{2(\gamma - 1)}} M_p \left[1 + \frac{\gamma - 1}{2} M_p^2\right]^{-\frac{\gamma + 1}{2(\gamma - 1)}} . \quad (2)$$

The other two regions are treated by the method of characteristics for the described flows. The compatibility relations for axisymmetric flows involves the independent position variable, r. They cannot be solved in closed form as is the case for two-dimensional plane flows, but can be solved by a numerical technique where the terms which involve the variable, r, are considered as correction terms which modify the two-dimensional solution and adjust it to the axially symmetric case.

The impingement shock emanating from the wall separates the two axially symmetric regions. The well known oblique shock wave equations are used in conjunction with the characteristics equations to define the flows across the shock and to define the shape and position of the shock. An added complexity exists in the solution of the compatibility equations for the rotational flow region because the shock is curved and the entropy downstream of the shock varies from one streamline to another. The entropy variation must be taken into account in the numerical technique used to generate the theoretical flow field.

The finite difference equations for steady, axisymmetric, potential flows and for steady, axisymmetric, rotational flows are presented in Appendix A. These equations are based upon the method characteristics for these flows and are readily solved on computers.

Computation Scheme

A computer program, based upon this computation scheme to solve the governing equations for the flow model of Figure 5, has been developed. As is the nature of the method of characteristics, the computer program provides a step-by-step output which completely describes the flow from the conical nozzle exit to the tube wall. Because of an approximation which was incorporated into the axially symmetric, rotational flow region, all the solutions in this region cannot be considered exact. The numerical results of the analytical investigation were obtained using the CDC 6600 computer system at Redstone Arsenal, Alabama.

The numerical routine input includes the ratio of specific heats for the gas, γ, and the nozzle geometry, r^*, r_e, and θ_n, and calculates the flow conditions at the lip of the nozzle exit. The pressure in the dead air region or base pressure is an input. This pressure must be obtained from actual tests or from an ancillary computation method and must be less than the exit pressure. The Mach number is determined using the base pressure/total pressure ratio in the isentropic pressure relation and the turning angle of the flow is determined using the

Prandtl-Meyer function. The flow turning angle at the corner is divided into equal increments, and the values $(\nu + \theta)$ and directions $(\theta - \mu)$ of the right running characteristics which define the expansion fan are calculated for each increment. The flow angle and Mach number of the inviscid flow boundary and the right running characteristics emanating from the nozzle lip are thus determined.

Now a new position in the conical flow region side of the expansion fan is determined by projecting a radius, R_p, of angle, $\theta_n - \Delta\theta$, (where $\Delta\theta$ is small) until it intersects the first right running characteristic. This is a simple trigometric calculation. By knowing R_p, the Mach number can be calculated by the stream tube relation and the values $(\nu - \theta)$ and direction $(\theta + \mu)$ of the left running characteristic can be determined. This method is also used to determine the characteristics in front of the shock wave, if the shock wave projects into the conical flow region instead of the expansion fan. A new right running characteristic is also defined for this point. This procedure is relatively simple and provides the same solution as constructing an axisymmetric characteristics net from the nozzle exit surface to the expansion fan or shock, whichever is adjacent to the conical flow region.

The left running characteristic is projected through the expansion fan to the jet boundary by the method of characteristics for axially symmetric, potential flow. At each point in the flow and on the jet boundary, new right running characteristics are determined. The computation method used is taken from Owczarek [24]. The left running characteristics are projected from the conical flow region side of the expansion fan until the jet boundary intersects the tube wall. The jet boundary flow characteristics (i.e., primarily, the flow angle because the Mach number is determined from the base pressure) at the wall intersection are determined by interpolation. As the jet boundary reaches the wall it is assumed to turn parallel to the wall, thus creating an oblique shock. The oblique shock equations are solved to determine the Mach number behind the shock at the impingement point and the total pressure drop across the shock wave for the wall streamline ($dS = 0$ for a streamline on either side of the shock wave). The shock wave angle with respect to the wall is also determined.

A new left running characteristic is initiated at the expansion wave and is projected into the potential flow region until the impingement shock is intercepted. The conditions in front of the shock are determined by interpolation. Figure 6 shows a construction of the characteristics net in front of the impingement shock.

A new shock angle and the conditions behind the shock and along the wall in the rotational flow region are determined by the method detailed in Appendix B. The flow angle in the conical flow region is decreased by $\Delta\theta$, left running characteristics are projected to the shock, and the conditions in the rotational flow region are calculated until $\theta_n - m\Delta\theta = 0$ (i.e., the nozzle centerline is reached). If the impingement shock projects into the conical flow region, the conditions in front of the shock are determined from the conical flow equations because the streamline does not pass through the potential flow region. A characteristics net in the rotational flow region is shown

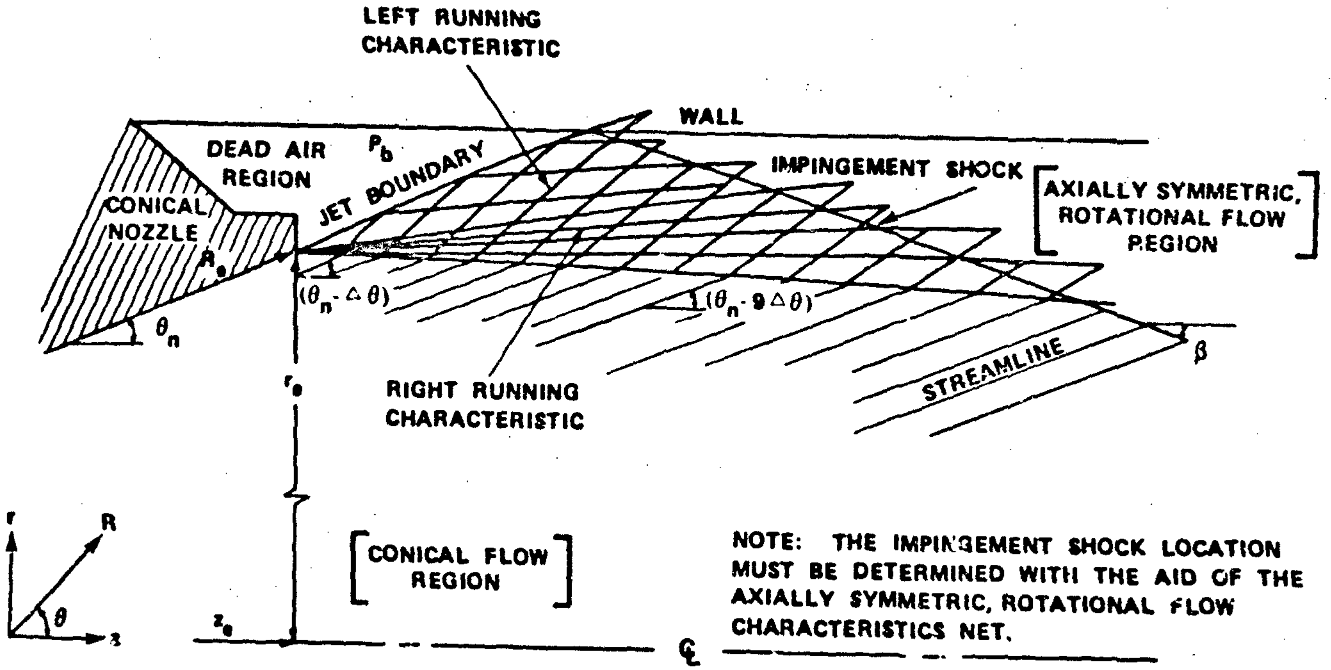
LEFT RUNNING CHARACTERISTIC
WALL
DEAD AIR REGION
P_b
JET BOUNDARY
IMPINGEMENT SHOCK
AXIALLY SYMMETRIC, ROTATIONAL FLOW REGION
CONICAL NOZZLE
R_e
θ_n
$(\theta_n - \Delta\theta)$
$(\theta_n - 9\Delta\theta)$
β
STREAMLINE
r_e
RIGHT RUNNING CHARACTERISTIC
r
R
θ
z
z_e
CONICAL FLOW REGION
℄
NOTE: THE IMPINGEMENT SHOCK LOCATION MUST BE DETERMINED WITH THE AID OF THE AXIALLY SYMMETRIC, ROTATIONAL FLOW CHARACTERISTICS NET.

Figure 6. Characteristics Net for Axially Symmetric, Isentropic Flow Region

in Figure 7. In reality, the characteristics are curved, but because of the method used, only the average angle is shown.

In the rotational region, a complete characteristics net is not used. Because of the entropy gradient normal to the streamlines, the streamlines must be followed to fully evaluate the flow and to construct a complete characteristics net. To simplify the computation in this region, the characteristics net from the wall streamline [$dS = 0$, $\theta = 0$, $\nu = f(z)$] to the streamline at the shock is constructed. This involves a calculation technique that is simpler than following the streamline and constructing a complete net but provides results which are not as exact. The accuracy of the output degrades proportionally with distance along the wall downstream from the shock or along the shock as the tube axis is approached. The accuracy is discussed in detail in Appendix B. Because of this simplification, the flow conditions in the region behind the shock cannot be determined to the tube axis, and the reflected shock or conditions behind it cannot be ascertained. The pressure immediately behind the impingement shock is "exact" according to the numerical technique and assumptions. Because the maximum wall pressure is assumed to be that immediately behind the impingement shock, an accurate calculation of this pressure is necessary for the objectives of this study.

It was hoped that some insight into the flow aft of the shock could also be obtained through this analytical technique.

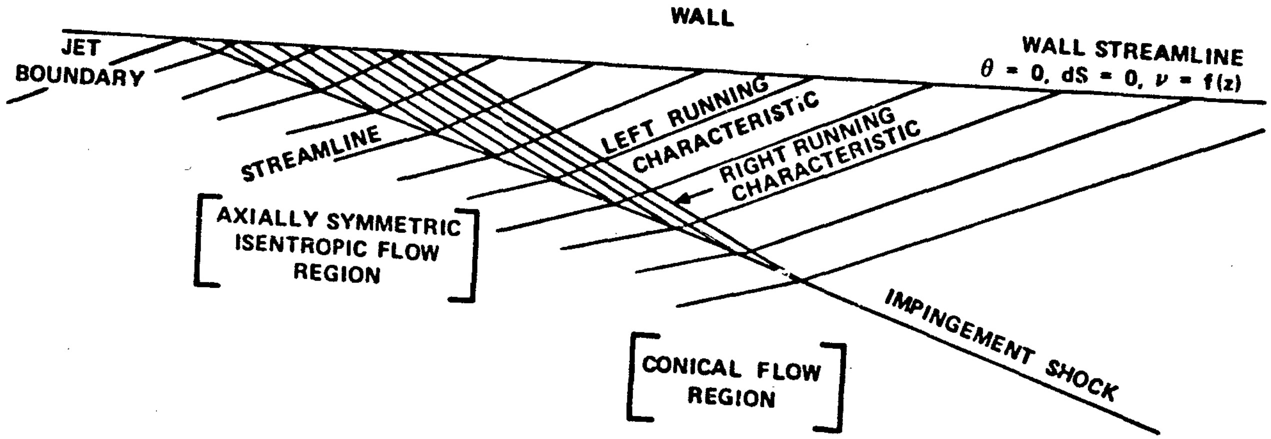
WALL
JET BOUNDARY
WALL STREAMLINE
$\theta = 0,\ dS = 0,\ \nu = f(z)$
STREAMLINE
LEFT RUNNING CHARACTERISTIC
RIGHT RUNNING CHARACTERISTIC
AXIALLY SYMMETRIC ISENTROPIC FLOW REGION
IMPINGEMENT SHOCK
CONICAL FLOW REGION

Figure 7. Characteristics Net for Axially Symmetric, Rotational Flow Region

CHAPTER IV

EXPERIMENTAL INVESTIGATION

General

A total of 48 cold flow and 8 hot flow (actual static rocket firings) tests were conducted to study experimentally the supersonic flow field in the cylindrical tubes. These tests consisted of exhausting an underexpanded, supersonic jet (i.e., $P_e > P_a$) from a stationary conical nozzle into a 2.558-inch internal diameter tube. Actually, a total of seven tubes were used to simulate the geometry with the rocket at various stations in the launcher. The tube lengths ranged from 0.7 to 6.2 tube internal diameters. Since the assumptions of the theoretical analysis more closely represent the cold gas experiments, the majority of the tests conducted were cold gas tests.

The nominal diameter of the nozzle exit for each type test was 2.1 inches which provides a relatively small ratio of tube radius to nozzle exit radius, $r_t/r_e = 1.2$. Test times were relatively short, i.e., approximately 10 milliseconds for the rocket firings and 300 milliseconds for the cold gas tests. High frequency response pressure transducers were used to determine the flow characteristics within the tube. Of particular interest from the launcher design viewpoint were the maximum wall pressures. Static wall pressures were obtained along the tube length. Special effort was made to locate instrumentation at the intersection of the shocks with the wall and, thus, obtain maximum wall pressures and an insight to the shock structure.

Pitot pressures were recorded during the cold flow tests by insertion of a pitot rake into the aft portion of the tube. By varying the length of the tubes, the flow may be probed in the longitudinal flow direction. The flow was also probed in the transverse direction. The pitot rake was used primarily to experimentally characterize the nozzle flow in the conical flow region. High speed pictures were obtained of the flow exiting from the tube to aid in the analysis of the flow within the tube.

Test Apparatus and Instrumentation

A photograph of a typical cold gas test setup is shown in Figure 8. Note that the pitot rake is positioned outside the tube. Pitot pressures were not obtained during the hot flow tests. The black and white striped board in Figure 8 is a background for the cameras. The camera coverage for both type tests (cold and hot flow) consisted of two cameras, a high speed 16-mm Fastax camera running at 3000 to 4000 frames/second and a 70-mm Hulcher camera sequencing at 20 frames/second. Color film was used in both cameras.

The cold gas facility with nozzle and tube in place is shown in Figure 9. The facility consists essentially of the motor, double burst diaphragms, reservoir, and chamber. Before operation, the reservoir and chamber volumes (0.5 cubic foot) are charged by remote control with dry nitrogen. Instrumentation for the operational control of the facility consists of four strain-gage pressure transducers (Baldwin

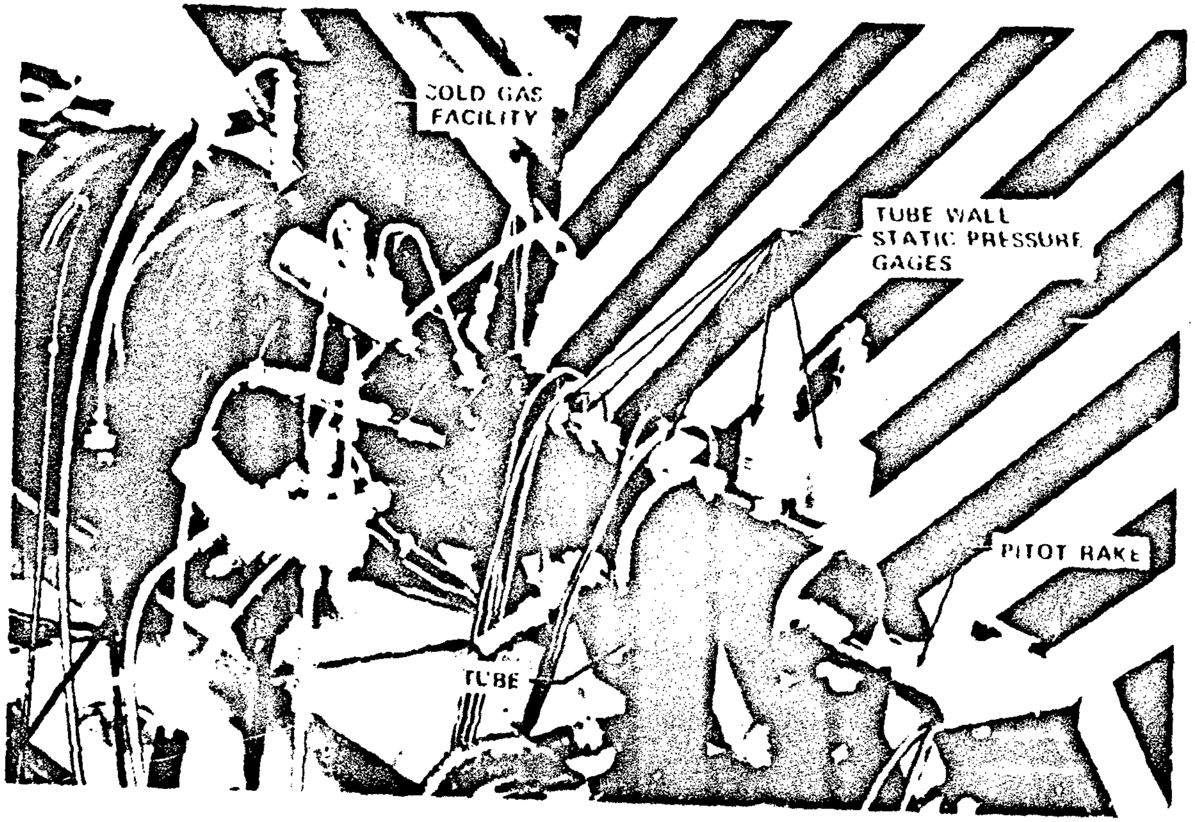
COLD GAS FACILITY
TUBE WALL STATIC PRESSURE GAGES
PITOT RAKE
TUBE

Figure 8. A Typical Cold Gas Test Setup

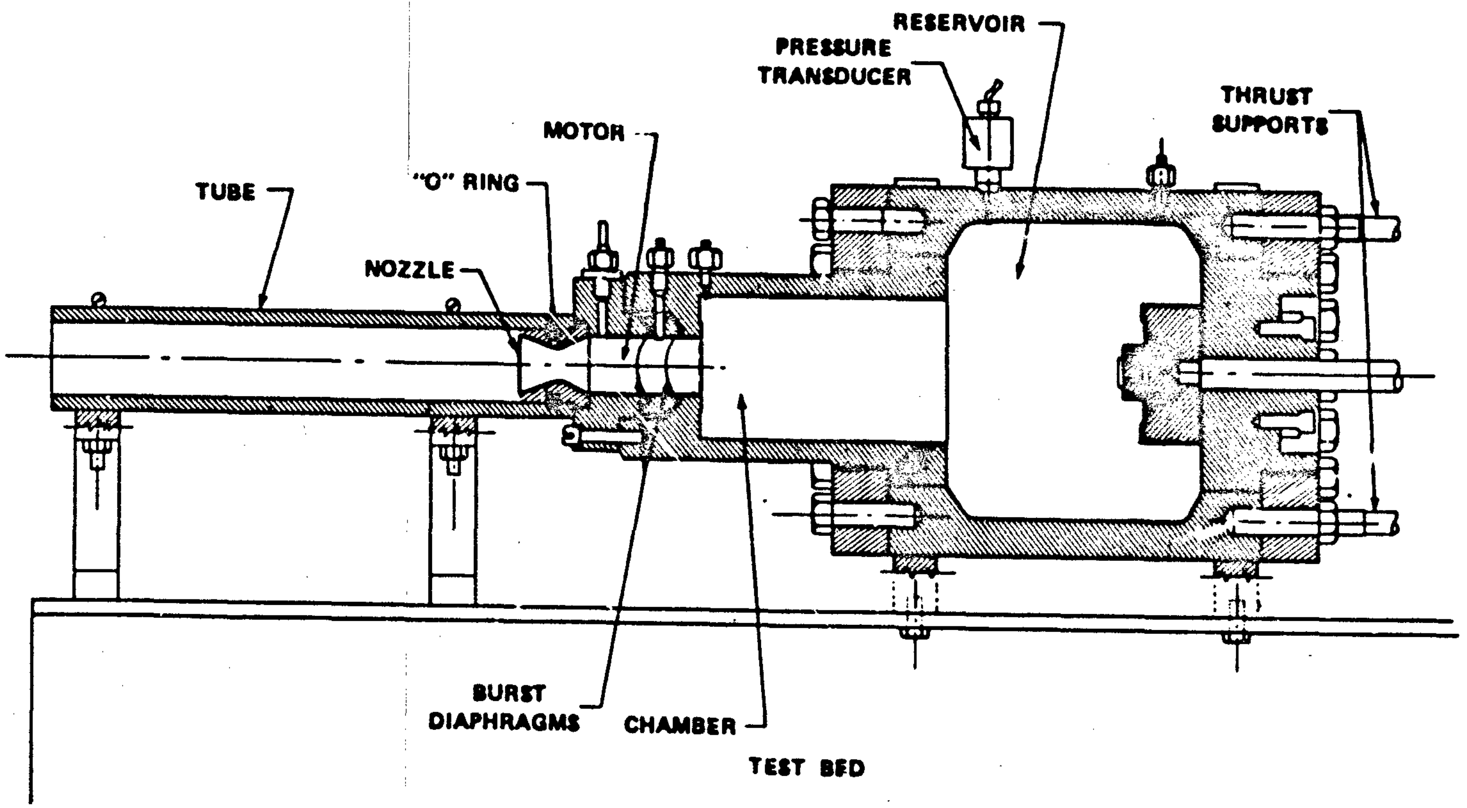
RESERVOIR
PRESSURE TRANSDUCER
THRUST SUPPORTS
MOTOR
"O" RING
TUBE
NOZZLE
BURST DIAPHRAGMS
CHAMBER
TEST BED

Figure 9. Cold Gas Facility with Nozzle and Tube in Place

gages having a 5000-psig maximum pressure) which sense pressures in the reservoir, in the chamber, in the space between the burst diaphragms, and in the motor section. Tests are initiated by a double-diaphragm technique. The gas in the reservoir and chamber then flows through the nozzle like a blow-down wind tunnel.

Initiation by the double-diaphragm method was accomplished as follows:

The reservoir and chamber were pressurized to a 4020 ±20 psia. At the same time, the space between the burst diaphragms is pressurized to 2020 ±20 psia so that at no time will the pressure differential across either diaphragm be greater than the diaphragm burst pressure. The gas between the diaphragms is then evacuated into the motor until the pressure differential across the first diaphragm exceeds the rupture pressure. The second diaphragm then ruptures allowing blow down through the nozzle.

The scored stainless steel burst diaphragms were designed and obtained commercially. The diaphragm rupture pressure was between 2375 and 2625 psi.

The conical convergent-divergent nozzle is attached to the short motor section which is located aft of the burst diaphragms (Figure 9). Notice the "O" ring which is used to prevent leakage between the nozzle and the forward section of the tube. In the case of the hot gas tests, two "O" rings were used. It was noted by Goethert [8], that leakage around the nozzle affects the base pressure. The rockets used in the hot gas tests had a conical convergent-divergent nozzle similar to the nozzle used in the cold gas tests. The nozzle geometry and gas characteristics for both nozzles are presented in Table I.

Table I. Nozzle Geometry and
Gas Characteristics

Parameter	Cold Gas Nozzle	Rocket Nozzle
γ	1.4	1.23
Throat Diameter (inches)	1.126	0.865
Exit Diameter (inches)	2.084	2.065
Divergence Cone half-angle (degrees)	20	20
Mach Number Exit	2.777	2.941
P_e/P_0	0.03815	0.02493

A typical hot gas setup is depicted in Figure 10. Double-base solid propellant rocket motors were used in the hot gas tests. These particular motors burn efficiently at a temperature of approximately 5000°F. These qualities (efficient burning at a relatively low temperature), in conjunction with the short burning time, minimize the heat transfer and real gas effects (which include afterburning).

The motor head closure was replaced for the static tests by a pressure/thrust adapter shown in Figure 10. The adapter facilitated

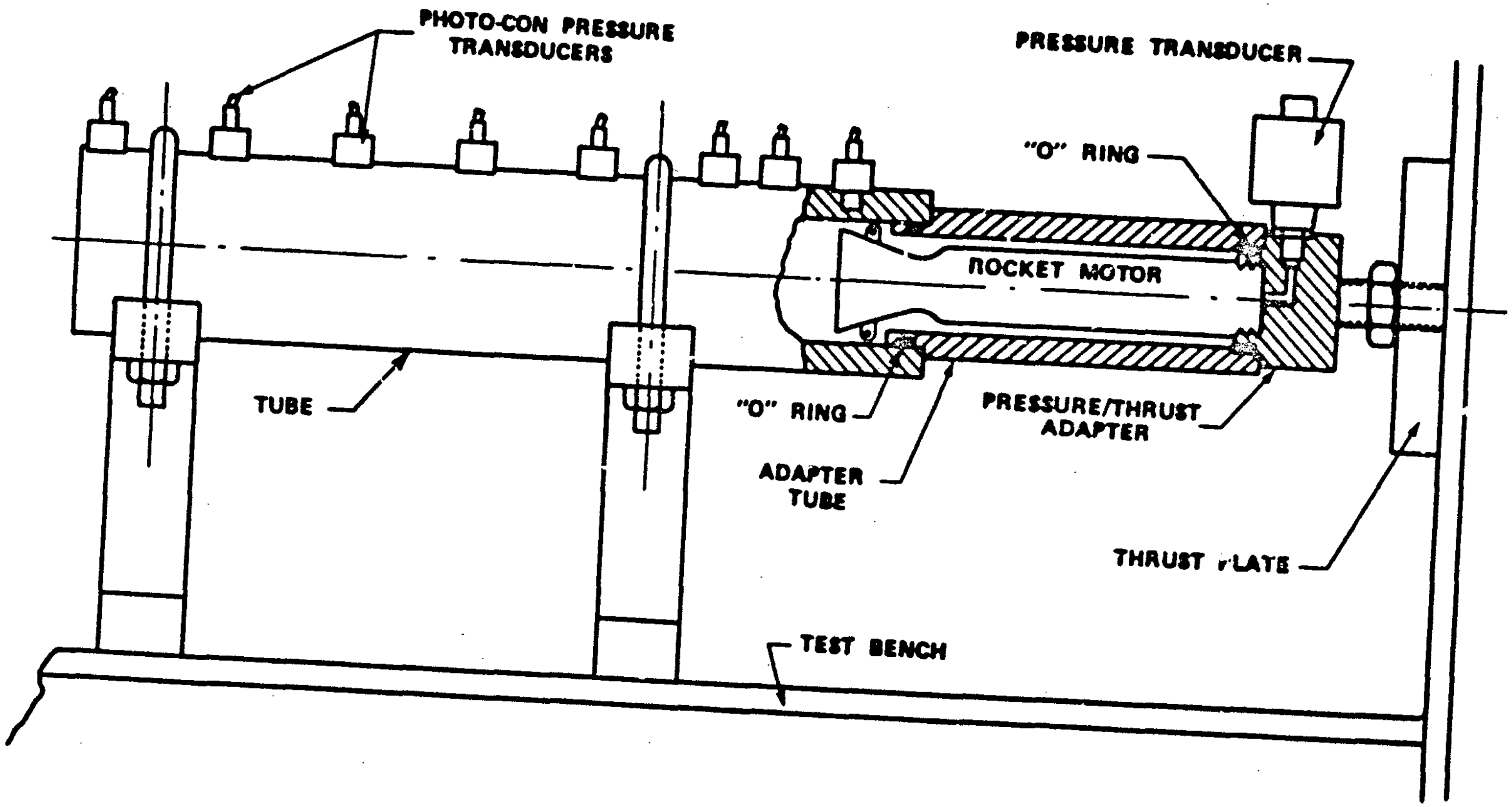
PHOTO-CON PRESSURE TRANSDUCERS
PRESSURE TRANSDUCER
"O" RING
ROCKET MOTOR
TUBE
"O" RING
PRESSURE/THRUST ADAPTER
ADAPTER TUBE
THRUST PLATE
TEST BENCH

Figure 10. Typical Hot Gas Test Setup

static firing and the measurement of the motor chamber pressure which was sensed by a 5000-psig maximum pressure Baldwin gage. The existing nylon nozzle-closure was replaced with an friable closure constructed of styrofoam to eliminate flow interference caused by the closure passing through the tube.

Seven tubes were manufactured according to the drawing in Figure 11. The station dimensions in Figure 11 were non-dimensionalized in terms of the tube inside diameter and were referenced to the nozzle exit plane. The ports along the top of the tubes were provided for the wall static pressure transducers. Section A indicates the stations where wall static pressures are taken around the circumference of the tubes. A typical static pressure port is also shown. A 1/8-inch diameter by 0.150-inch long port separates the transducer pressure sensing surface from the tube wall. The edges of the orifices were deburred to minimize flow interference. The relatively large port diameter was needed to maintain the required response time. Two types of strain-gage pressure transducers, i.e., 2000-psig maximum pressure Photo-Cons and 500-psig maximum pressure Baldwins, were used to obtain tube wall static pressures. These gages were screwed into the threaded portion of the port. Sealing was accomplished by torquing the gage bodies against an aluminum ring. The enlarged void immediately in front of the pressure sensing surface was less than 0.005-inch long.

During the course of testing, it was found that static pressure data were required at other positions along the tube wall. Subsequently, the tubes were modified to incorporate additional pressure transducers. Table II lists these additional pressure port

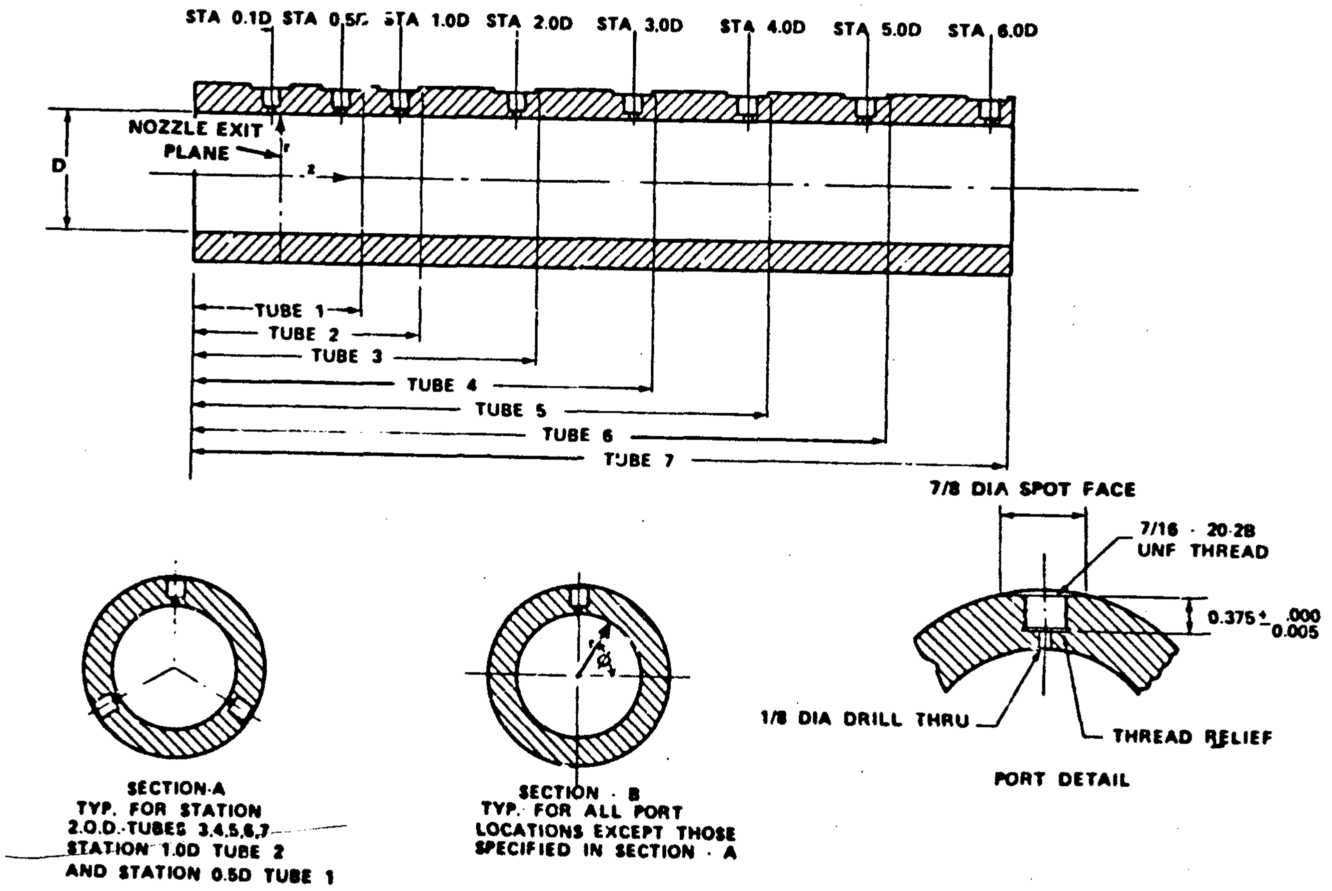
STA 0.1D
STA 0.5D
STA 1.0D
STA 2.0D
STA 3.0D
STA 4.0D
STA 5.0D
STA 6.0D
NOZZLE EXIT PLANE
D
r
z
TUBE 1
TUBE 2
TUBE 3
TUBE 4
TUBE 5
TUBE 6
TUBE 7
7/8 DIA SPOT FACE
7/16 - 20-2B UNF THREAD
0.375 +.000 -0.005
1/8 DIA DRILL THRU
THREAD RELIEF
PORT DETAIL
SECTION-A
TYP. FOR STATION 2.0.D.-TUBES 3,4,5,6,7
STATION 1.0D TUBE 2
AND STATION 0.5D TUBE 1
SECTION - B
TYP. FOR ALL PORT LOCATIONS EXCEPT THOSE SPECIFIED IN SECTION - A
φ

Figure 11. Cylindrical Tubes Showing Static Pressure Port Detail and Static Pressure Locations (Series A)

positions. Consequently, two series of tubes are designated. Series A consists of the tubes with port positions as depicted in Figure 11, and series B consists of the same tubes with the added ports according to Table II.

Table II. Additional Tube Wall Static
Pressure Positions
(Series B)

Tube	z Position (ID)	ϕ (deg)
1	0.1	60
	0.3	120
3	1.5	90
4	2.25	135
	2.50	45
	2.75	180
5	3.25	135
	3.50	45
	3.75	180
6	4.25	135
	4.50	45
	4.75	180
7	5.25	135
	5.50	45
	5.75	180

Two views of the pitot rake in situ are shown in Figure 12. The adjustable mount allows the rake position to be varied relative to the tube in the axial and radial directions. Note that in this drawing the probes are positioned within the tube. The rake consists of three square faced 1/8-inch outside diameter cylindrical tubes mounted along the edge of a 17-1/2-degree half angle wedge. The diameter of the hole in the face of each probe was 0.040 inch and provides a ratio of hole diameter to cylinder outside diameter of 0.32. The tubes are positioned horizontally as shown and project 0.61-inch forward from the wedge edge. A shroud is attached to protect the pressure transducers which screw into the aft end of the wedge. The pitot pressures were sensed by 2000-psig maximum pressure Photo-Con strain-gage type pressure transducers. The tube distance to the pressure sensing surface of the gage was 1.61 inches with the enlarged void immediately in front of the pressure sensing surface being less than 0.005-inch long. These distances were kept at a minimum to insure adequate time response. Sealing was accomplished by torquing the gage bodies against an aluminum ring.

Test Description

Pertinent information regarding each test is presented in Table III. The tube wall static pressure locations are not given. However, in every case, wall static pressures were recorded at each port location. These locations for each tube are defined in Figure 11 and Table II. By slightly moving the tube in the axial direction, all the port locations relative to the nozzle exit are changed such as for

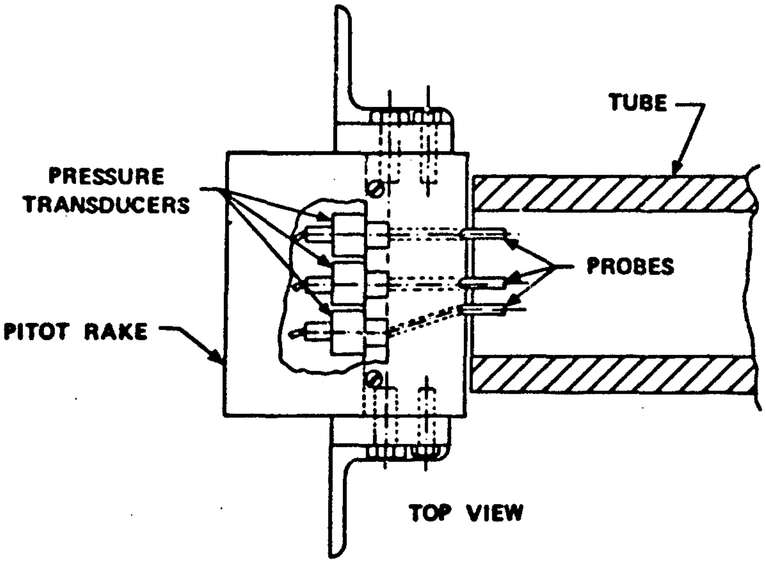
TUBE
PRESSURE TRANSDUCERS
PROBES
PITOT RAKE

TOP VIEW

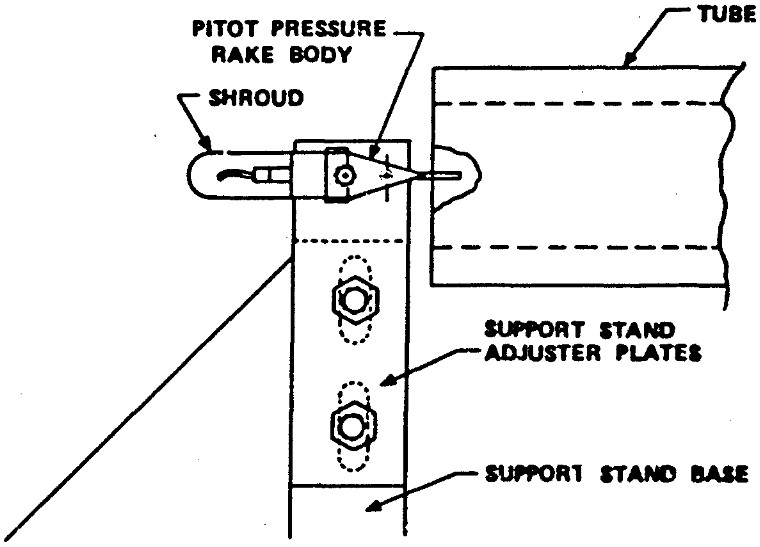
TUBE
PITOT PRESSURE RAKE BODY
SHROUD
SUPPORT STAND ADJUSTER PLATES
SUPPORT STAND BASE

SIDE VIEW

Figure 12. Three Probe Pitot Rake

Table III. Experimental Program Summary

Test	Cold	Hot	Tube	Tube Position	Pitot Position
			Preliminary Tests		
1		X	No	NA	PNU
2		X	No	NA	PNU
3	X		No	NA	Nozzle exit
4	X		No	NA	Nozzle exit
5	X		1a*	Normal	0.5-in. in tube
6	X		1a*	Normal	Tube exit
7	X		1a*	Normal	PNU
8	X		3a*	Normal	Tube exit plane
9	X		3a*	Normal	Tube exit plane
			Tests		
10	X		No	NA	Nozzle exit
11	X		No	NA	0.22-in. aft nozzle exit

* Not sealed between nozzle and tube

PNU — Pitot not used
NA — Not applicable

Table III. Continued

Test	Cold	Hot	Tube	Tube Position	Pitot Position
12	X		No	NA	1.281-in. aft nozzle exit
13	X		No	NA	2.558-in. aft nozzle exit
14	X		No	NA	5.116-in. aft nozzle exit
15	X		No	NA	7.674-in. aft nozzle exit
16	X		No	NA	10.232-in. aft nozzle exit
17	X		No	NA	12.790-in. aft nozzle exit
18	X		No	NA	15.348-in. aft nozzle exit
19	X		1a	0.25-in. aft	0.5 in. in tube
20	X		1a	Normal	0.5 in. in tube
21	X		1a	Normal	0.5 in. in tube
22	X		1a	Normal	0.5 in. in tube

NA — Not applicable

Table III. Continued

Test	Cold	Hot	Tube	Tube Position	Pitot Position
23	X		1a	Normal	Outside tube
24	X		7a	Normal	0.5 in. in tube
25	X		7a	Normal	Tube exit
26	X		1a	Normal	0.5 in. in tube
27	X		2a	Normal	0.5 in. in tube
28	X		2a	Normal	0.5 in. in tube
29	X		2a	Normal	Outside tube
30	X		3a	Normal	0.5 in. in tube
31	X		3a	Normal	Outside tube
32	X		4a	Normal	0.5 in. in tube
33	X		4a	Normal	Outside tube
34	X		5a	Normal	0.5 in. in tube
35	X		5a	Normal	Outside tube
36	X		6a	Normal	0.5 in. in tube
37	X		6a	Normal	Outside tube

Table III. Continued

Test	Cold	Hot	Tube Tests	Tube Position	Pitot Position
38	X		3b	Normal	PNU
39	X		4b	Normal	PNU
40	X		4b	0.263 in. aft	PNU
41	X		5b	Normal	PNU
42	X		6b	Normal	PNU
43	X		6b	0.263 in. aft	PNU
44	X		7b	Normal	PNU
45	X		1b	Normal	PNU
46	X		1b	0.406 in. aft	Tube exit
47	X		No	NA	Nozzle exit
48	X		No	NA	1.0-in. aft nozzle exit
49		X	1b	Normal	PNU

PNU — Pitot not used
NA — Not applicable

Table III. Concluded

Test	Cold	Hot	Tube	Tube Position	Pitot Position
50		X	1b	0.25-in. aft	PNU
51		X	4b	Normal	PNU
52		X	7b	Normal	PNU
53**	X		1b	Normal	PNU
54**	X		2b	Normal	PNU
55		X	1b	Normal	PNU
56		X	1b	0.125 in. aft	PNU

** Only camera data obtained

PNU — Pitot not used
NA — Not applicable

test 19. This was done to provide additional pressure data and to define the pressure distribution without the addition of more orifices and instrumentation. The pitot probe positions in the flow direction are given. However, the transverse positions of the pitot probes are not given but will be indicated when the data are presented.

Preliminary tests were conducted to check out the operation of the cold gas facility and instrumentation. Note that for these tests, the "O" ring was not positioned between the nozzle and tube wall to seal the dead air region from the atmosphere. These tests also provided information regarding the magnitude and variation of static pressures along the tube wall. This information was used to calibrate the pressure gages over the ranges indicated so that the best accuracy could be obtained.

Two rockets were static fired to determine if reliable chamber pressure could be obtained. To obtain pressure at the head end of the rocket motor, the propellant pin plate, which is between the propellant and the pressure gage, had to be filled with holes. Of concern was the effect of this restriction on obtaining adequate pressure time response. Upon comparison of thrust data with the pressure data, it was found that this modification was adequate. The friable nozzle closure was also checked at this time.

A total of 13 cold gas tests were conducted with the nozzle exhausting into the atmosphere, i.e., without tubes. These exhaust flows were probed with the pitot rake at various positions in the flow. This information was used to ascertain the type of flow provided by the conical nozzle.

The remainder of the tests were conducted with tubes. Test density per type test per tube is presented in Table IV. Pressure data

Table IV. Test Density Per Type
Test Per Tube

Tube		Hot Gas	Cold Gas		
		No. of Tests	No. of Tests		
		No Pitot	No Pitot	Pitot Outside Tube	Pitot in Tube
1	A		1	2	6
	B	4	2	1	0
2	A		0	1	2
	B		1	0	0
3	A		0	2	2
	B		1	0	0
4	A		0	1	1
	B	1	2	0	0
5	A		0	1	1
	B		1	0	0
6	A		0	1	1
	B		2	0	0
7	A		0	1	1
	B	1	1	0	0
TOTALS		6	11	10	14

NOTE: Atmospheric tests; 13 cold gas, 2 hot gas.

for tests 53 and 54 were not obtained as these tests were conducted to obtain better pictorial coverage of the impingement shock. Most of the tests were conducted with tube 1. This tube, which was the shortest and for which the pressure ports were concentrated near the jet boundary-wall intersection, allows the flow near the impingement shock to be investigated with the pitot rake. Two other pressure peaks were noted in the cold gas flows. Hence, numerous tests with tubes 4 and 6 were conducted to define the flow conditions or causes of the peaks.

To give a better wall pressure representation, the A-series tubes were altered to provide more data points. Tests 38 through 56 were conducted with the altered tubes, designated B series. The Hulcher sequencing camera was incorporated into the instrumentation for these tests. Because of the limitation of available rockets, only eight hot gas tests were conducted including the two preliminary tests. Consequently, most of the effort was directed toward obtaining wall pressures in tube 1. Although tests were run with tubes 4 and 7 to obtain an idea of the pressure conditions along the wall, the test times for the hot gas tests were too short to obtain 70-mm camera coverage.

Data Reduction and Discussion of Test Data

For the cold flow tests, the pressures sensed by the transducers were recorded on tape and on Consolidated Electronic Corporation oscillograph recorders. The recorders were run at 160 inches/second. The gages were calibrated in the required pressure range before a series of tests. The maximum pressure to be sensed by each gage was estimated and this pressure was established as the required range. This range was projected as full scale on the recorder to obtain the maximum resolution possible.

The data recorded on the tape was transcribed from analog to digital form so that it could be reduced to engineering units by the CDC 6600 computer. The computer program, which was written to reduce the data, also performed necessary calculations (viz, averaging, nondimensionalizing, and Mach number calculations). To obtain the best accuracy possible, the zero shifts which were noted on the oscillograph records were inputed to the computer program for correction. Because the velocities in the cold gas facility reservoir and chamber were small, the average of these two pressures were taken as the total pressure. All pressures were nondimensionalized by the total pressure.

The double burst diaphragm technique, which is also used in shock tubes, initiates a series of shocks and expansion waves which propagate into the tube. The time lag of the instruments when checked against these pressure pulses was nil. It was decided to reduce the data over that portion of the test which represented a near steady state and which was void of pressure discontinuities. Consequently, the data were analyzed over the time span of 0.023 to 0.073 second after flow initiation. The total pressure and typical wall pressure for test 19, showing time interval between reduced points and time span for which data were reduced, are presented in Figure 13.a. The computer program provided data over this time span in increments of 2.5 milliseconds. Although the total test run time was approximately

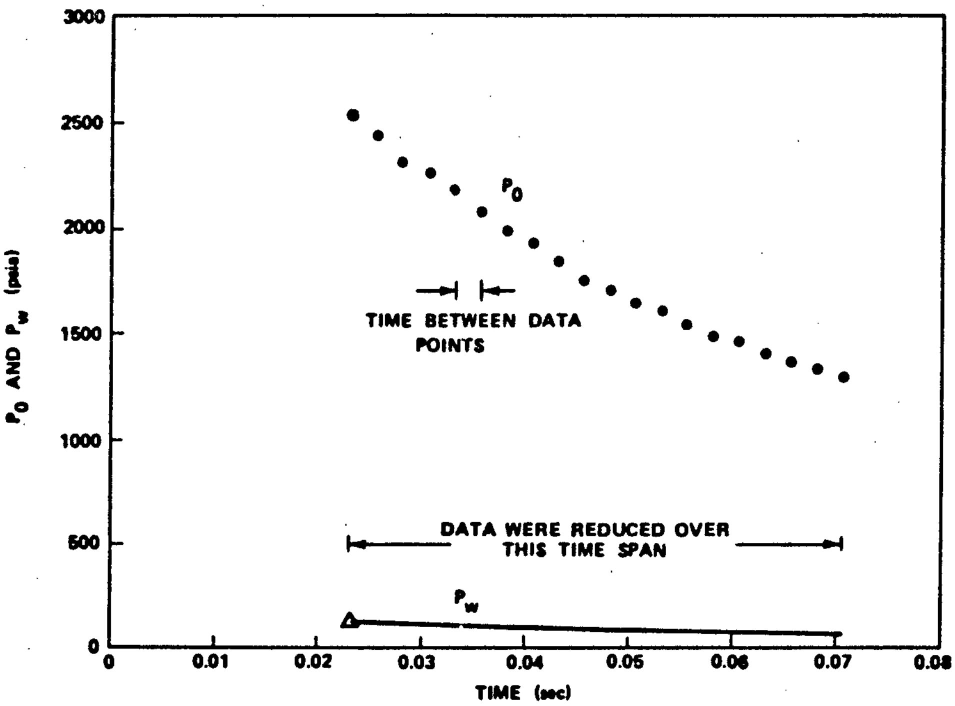

a. TOTAL PRESSURE AND TYPICAL WALL STATIC PRESSURE DATA

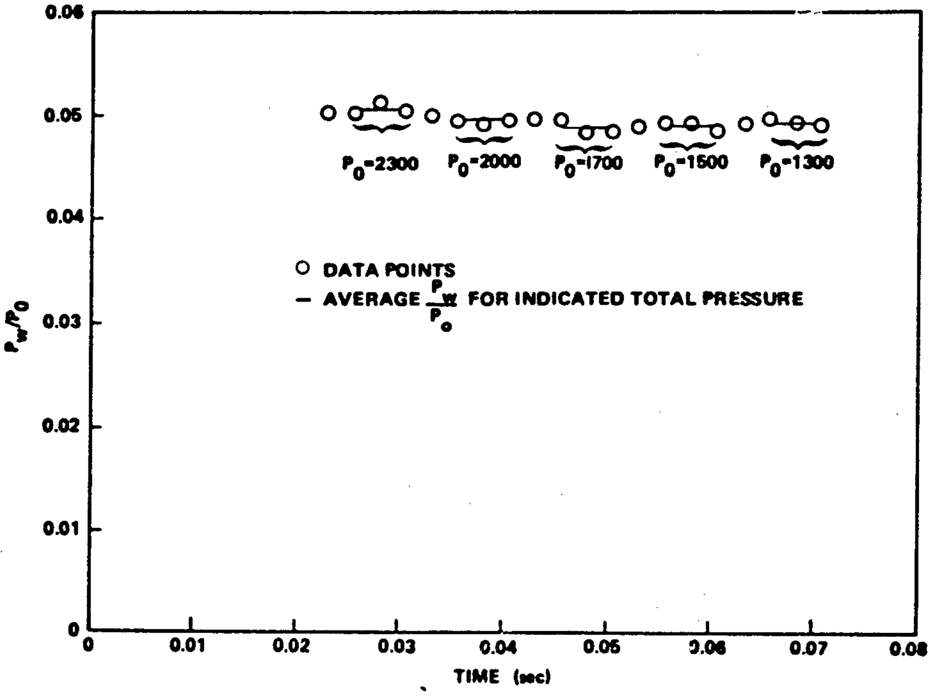

b. DIMENSIONLESS WALL STATIC PRESSURE DATA

Figure 13. Total Pressure and Typical Wall Pressure for Test 19 (Cold Gas Test)

0.3 second, the data were not reduced after 0.073 second to eliminate the reduction of data when condensation was present in the flow.

Based upon the literature survey, it is reasonable to assume that the conditions in the tube are independent of the nondimensionalizing parameter, P_0. With this in mind and for the ease of data analysis, only cold flow data corresponding to five total pressures are considered, i.e., P_0 = 2300, 2000, 1700, 1500, and 1300 psia. Because the reduced data may not provide information at these exact total pressures, the data presented represent an average of three total pressures, one on each side and the closest total pressure (Figure 13.b). Note the data to be averaged are already nondimensionalized. The time span over which these three pressures are recorded is 5 milliseconds which provides an adequate representation of the flow field for this time. The use of the average of the three values inherently tends to smooth the data. The Mach numbers were averaged as were the static wall pressures when a large variation in Mach number was noted. However, in most cases, the Mach number varied only a few hundredths and, in these cases, the Mach number presented is an average of all the values.

The use of the tape-computer system was not feasible to reduce the hot flow data because of the short test times. The hot flow data were directly reduced from the oscillograph records. Data representing three times that occurred during the motor operation were reduced. A typical pressure/time representation is shown in Figure 14. The pressure data were nondimensionalized with the motor chamber pressure. For hot gas experiments 55 and 56, the motor chamber pressures were markedly different from that shown in Figure 14. The pressures

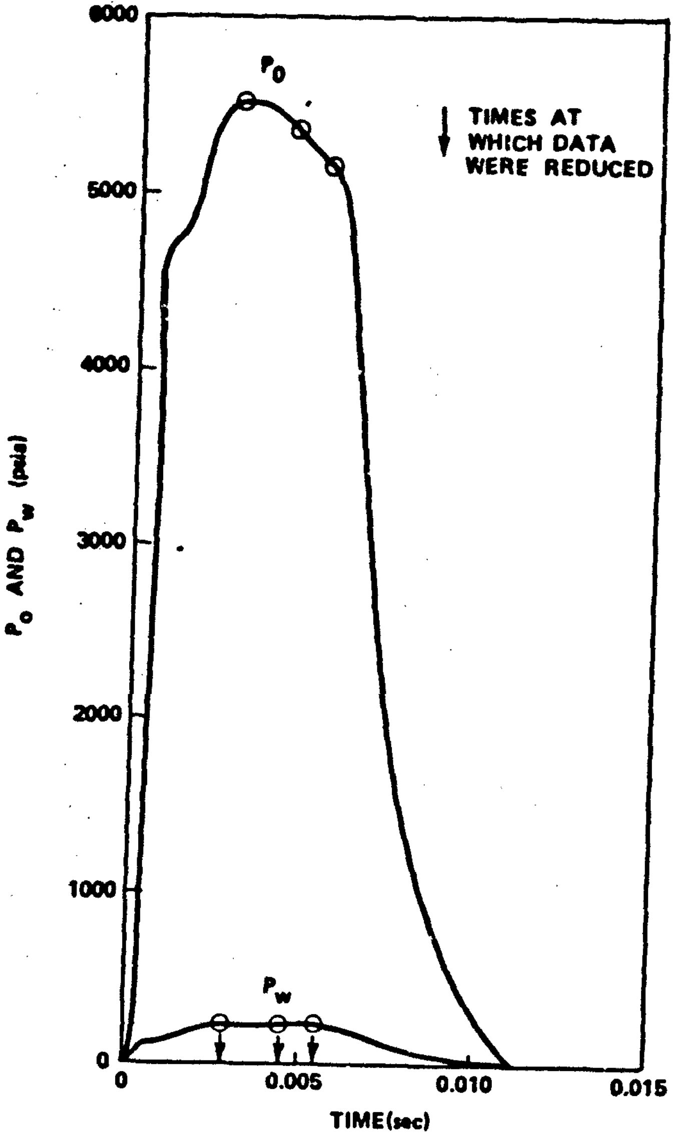

Figure 14. Typical Pressure/Time Representation For Hot Gas Test

peaked at approximately 6380 psia and were regressive in nature, over a shorter time. This occurred because the temperature of the propellant grains were higher than those of the other hot gas experiments.

The nondimensional data represents two pressure measurements - one divided by another - with individual accuracies (plus or minus a certain percent) which may be additive or nullifying. The accumulative error, or worst accuracy, is given. However, statistically, and in reality, the average error will be less. According to Gracey [25], a pitot probe of this design, i.e., with a ratio of hole diameter to probe outside diameter of 0.32, will be insensitive to an angle of attack of ±13-1/2 degrees. Because the static pressures in the tube vary as a function of radius, the Mach number of the flow downstream of the shocks cannot be determined from the pitot pressure and wall static pressures. Also, because of design flow angle limitation, the probes are limited to flow angles of less than ±13-1/2 degrees. A knowledge of the flow angle is required and was not obtained experimentally. Also, the ability of the pitot probe to accurately measure pitot pressure in a flow with a large radial flow gradient is in question. The overall accuracy of the pitot probe, including response time errors, instrument and positioning error, and the method of data reduction, but excluding flow angle and radial gradient sensitivities, is considered to be within ±6 percent. This amounts to a Mach number error of approximately ±3 percent. The error for the wall static pressures obtained in the cold flow tests is believed to be ±3-1/2 percent. The accuracy of the data in the hot gas is degraded, primarily as a result of the severity of the pressure and temperature gradients with respect to time imposed on the transducers and the resolution of data during reduction. This error can be as high as ±5 percent. The static pressure accuracies are based upon the response time, error of the data acquisition system, instrument error, zero shift, errors imposed by orifice edge form and port diameter, and errors due to the method of data reduction.

CHAPTER V

RESULTS AND DISCUSSION

Preliminary Remarks

Before any conclusions can be reached concerning the nature of the flow in the tube and the parameters which govern the flow, certain basic premises must be investigated and verified to ascertain the validity of the experimental methods and assumptions used in the theoretical analysis. Because of the method of testing, i.e., multiple tests with limited instrumentation per test, the repeatability of the flow conditions within the tube from experiment to experiment is paramount.

The initiation conditions and the time interval over which the cold flow data were obtained were standardized in an effort to reproduce the flows in the tube from experiment to experiment. This was also attempted for the hot gas rocket firings; however, two tests (55 and 56 as discussed previously) were inadvertently conducted at a different propellant conditioning temperature. The total pressures for these two tests were markedly different and required that the data be obtained over a different time span.

The correlation of the experimental results with those obtained by theoretical analysis depends upon how well the theoretical assumptions were duplicated during the experimental investigations. The character of the nozzle exhaust (underexpanded, supersonic, conical, and axisymmetric) and the symmetry of the flow in the tube were dependent on the constraints of the experiment and are, to a certain extent, controllable by the experimenter. The validity of the fully developed supersonic flow assumption upon which the flow model was developed and the quasi-steady flow assumption is dependent upon the results of the experiments.

Character of the Nozzle Exhaust

The Mach number in the nozzle exhaust was calculated from the total pressures behind a normal shock, as measured by the pitot probes, and the total pressure in front of the normal shock, as measured in the reservoir. The Mach numbers in the proximity of the nozzle exit were used to characterize the nozzle flow and to ascertain if the nozzle did, in fact, provide conical flow. Because pitot data were not obtained during the hot gas tests, only the cold gas nozzle exhaust characteristics can be presented.

Figure 15 presents the Mach number obtained from the pitot probes plotted with respect to the physical conical radius parameter, $(R-z_e)/r_e$. Zero represents the point on the nozzle centerline in the exit plane. Data are presented for the nozzle exhausting into the atmosphere and into tubes 1 and 2, in the vicinity of the nozzle exit. Also included is the theoretical curve for conical flow. Note that the data points, with the exception of the numbered points, fall along the theoretical curve. The physical positions of the probes are shown in Figure 16. Figure 16.a shows the salient features obtained from

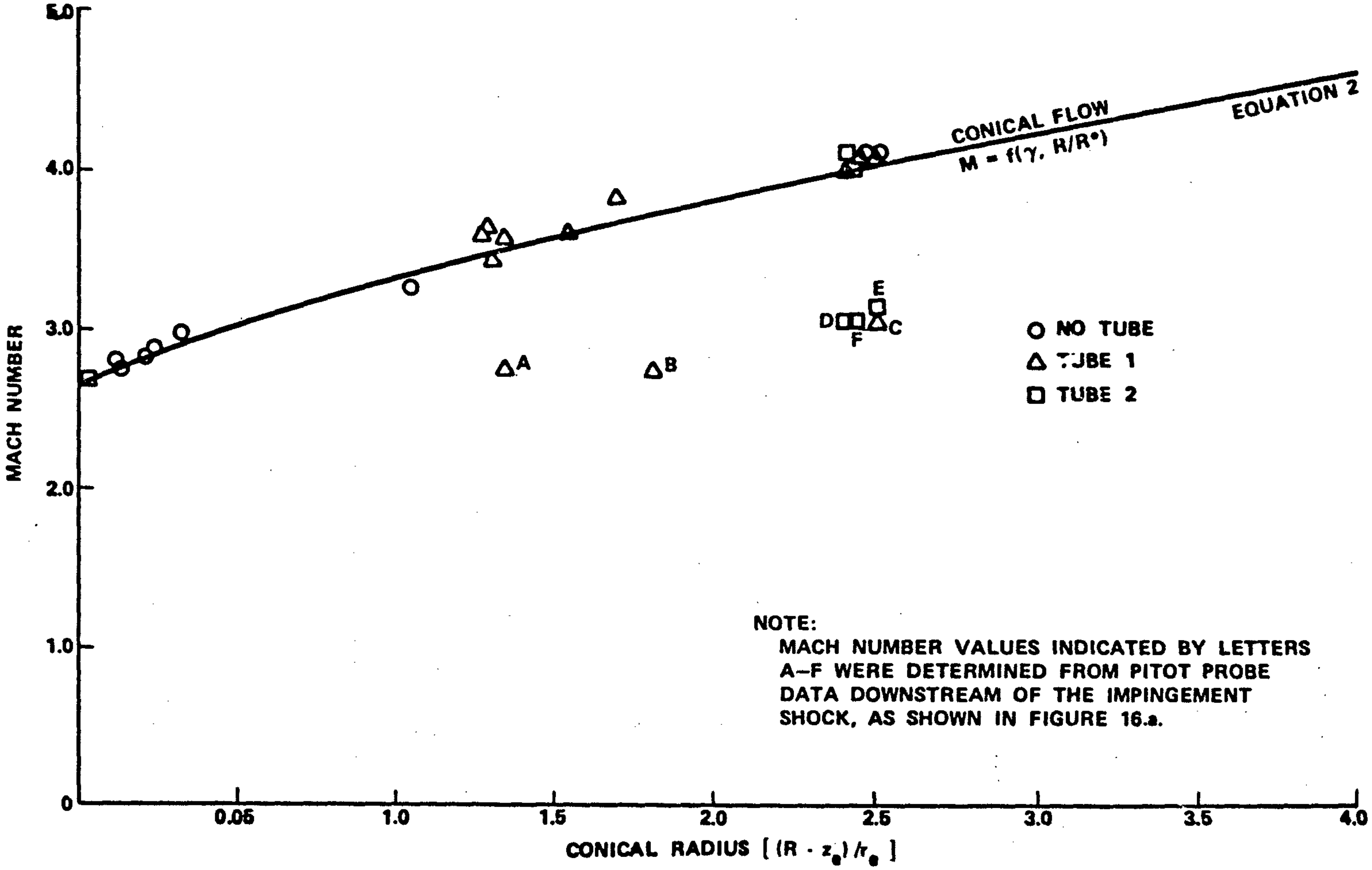

NOTE:
MACH NUMBER VALUES INDICATED BY LETTERS A–F WERE DETERMINED FROM PITOT PROBE DATA DOWNSTREAM OF THE IMPINGEMENT SHOCK, AS SHOWN IN FIGURE 16.a.

Figure 15. Cold Gas Nozzle Exhaust Mach Number Versus Conical Radius (Pitot Data)

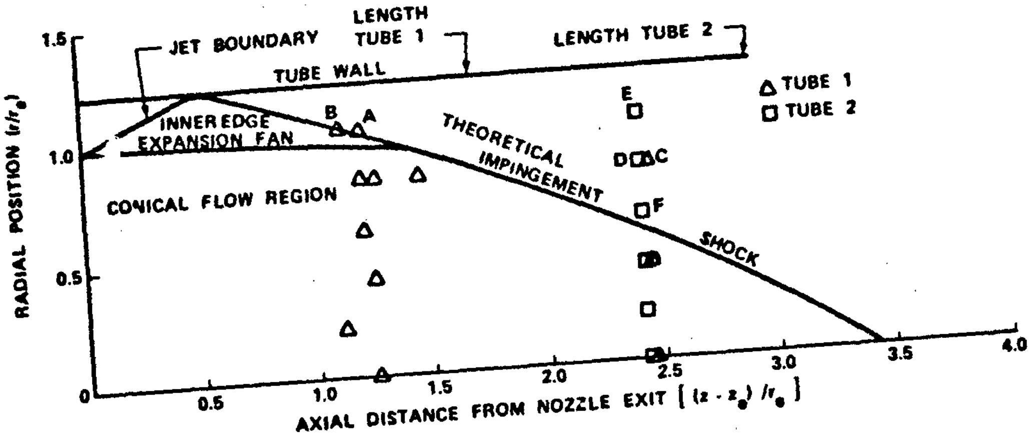

a. Pitot Probe Positions for Nozzle Exhausting into tubes 1 and 2

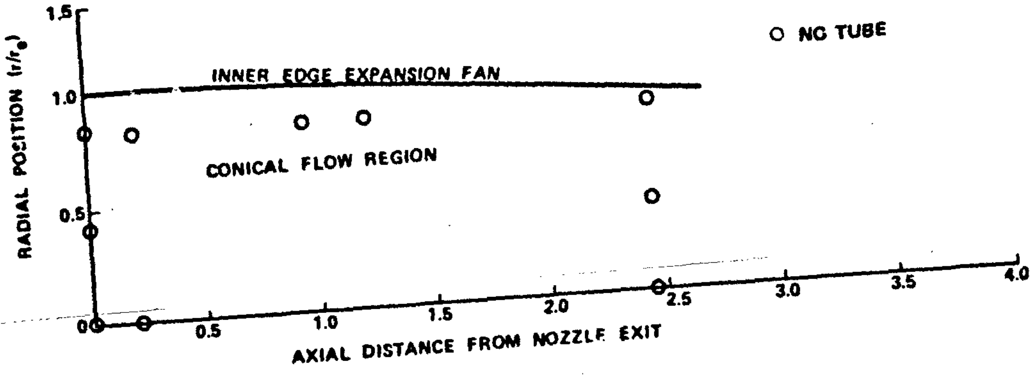

b. Pitot Probe Positions for Nozzle Exhausting into the Atmosphere

Figure 16. Physical Positions of the Pitot Probes in Nozzle Exhaust

the theoretical analysis ($P_b/P_0 = 0.0218$) which define the conical flow region for the nozzle exhausting in the tubes. The inner edge of the expansion fan which defines the conical flow region for the nozzle exhausting into the atmosphere is shown in Figure 16.b. The numbered points are either located on or downstream of the impingement shock outside of the conical flow region. Point C represents a pitot probe position for test 23. Figure 17 is a photograph taken from 16-mm film of this test condition. The impingement shock emanating from the tube and the normal shock induced by the presence of the pitot probes are evident in this photograph. The impingement shock is located inboard of the outboard pitot probe, data point C, and outside of the next probe as shown in Figure 16.a. The Mach number data from the points outside of the conical flow region are invalid because of the presence of the shock. However, they serve to give an indication of the physical bounds to the conical flow region.

Thus, it is seen that the nozzle provides conical flow in the vicinity of the exit. Because the pitot probes were located at different radial positions in the nozzle exhaust, it is also concluded that the nozzle provides flow which is axially symmetric. Because the Mach numbers as determined from the probe data were essentially constant over the entire data acquisition time span or total pressure range, the nozzle exhaust flow is independent of total pressure or time.

The constraints of the experimental control conditions, i.e., nozzle geometry coupled with total pressures, dictate that the nozzle exhaust is underexpanded with respect to the tube exit pressure, P_a. This does not assure that the nozzle exhaust into the tube with the

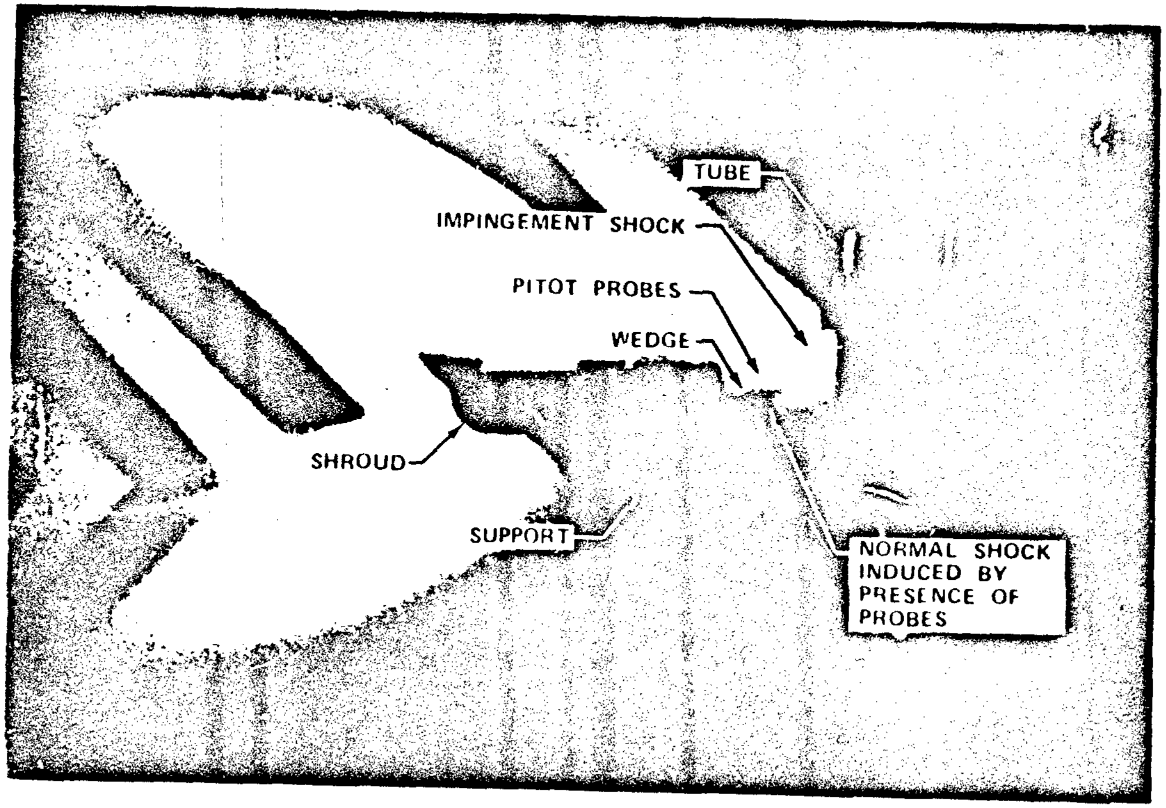
TUBE
IMPINGEMENT SHOCK
PITOT PROBES
WEDGE
SHROUD
SUPPORT
NORMAL SHOCK INDUCED BY PRESENCE OF PROBES

Figure 17. View Showing Impingement Shock Emanating from Tube and Normal Shock Induced by Pitot Probes for Test 23

unknown base pressure is underexpanded. This is the case, however, because the nozzle exit pressure is greater than the base pressure. The base pressure/nozzle exit pressure relations obtained during the cold and hot gas tests are presented in Table V.

Table V. Base Pressure/Nozzle Exit Pressure Ratios

Cold Gas Tests			Hot Gas Tests		
P_o (Psia)	$\frac{P_b}{P_o}$	$\frac{P_b}{P_e}$	P_o (Psia)	$\frac{P_b}{P_o}$	$\frac{P_b}{P_e}$
2300	.0218	.571	5440	.0066	.265
2000	.0225	.590	5350	.0073	.293
1700	.0231	.606	5135	.0082	.329
1500	.0239	.626			
1300	.0244	.640			

Quasi-Steady Flow

According to Korst et al. [19], the nozzle exhaust flow in the viscous shear layers that bound the dead air region along with the physical geometric contraints dictate the equilibrium base pressure by mass transfer into or out of the dead air region. And according to Ihrig and Korst [30], the ratio of adjustment time for the transfer of mass as compared to pressure disturbance adjustment time in the supersonic flow is approximately 30 for Mach 1 flow; i.e., the pressure field in the main flow adjusts almost instantaneously to the slower base pressure variation. According to Fabri and Siestrunck, the ratio

P_b/P_0 for supersonic fully developed steady flow is a constant. Korst also predicts a constant for steady flow, but allows for a variation in his quasi-steady analysis.

It is significant that the dimensionless base pressure increased with time for the cold and hot gas flows. However, there were two important parameters varing since an increase in time was accompanied by a decrease in total pressure. Because the total pressures occurred at approximately the same times during the tests for the cold flow data presented, the effects of the two parameters could not be separated. The total pressure histories were also duplicated for the majority of the hot gas tests. However, this was not the case for two hot gas tests (tests 55 and 56) which were conducted at a higher propellant temperature. The burning rate of the particular propellant varies with temperature; consequently, the total pressures for these tests were higher and the burning time was decreased. The base pressure is presented as a function of total pressure for the hot gas flows in Figure 18. The total pressures of the ordinate are reversed to give an indication of increase in time from left to right. This is because of the regressive burning characteristics of the rocket motors. Note that because of the shorter burning time of tests 55 and 56, the time derivative of the dimensionless base pressure of the two traces in Figure 18 would be approximately the same if the dimensionless back pressure was considered with respect to time.

The missile oriented base pressure computer program, as described by Addy [31], was altered to calculate the base pressure for the sudden expansion of an axisymmetric jet into a shroud for the zero

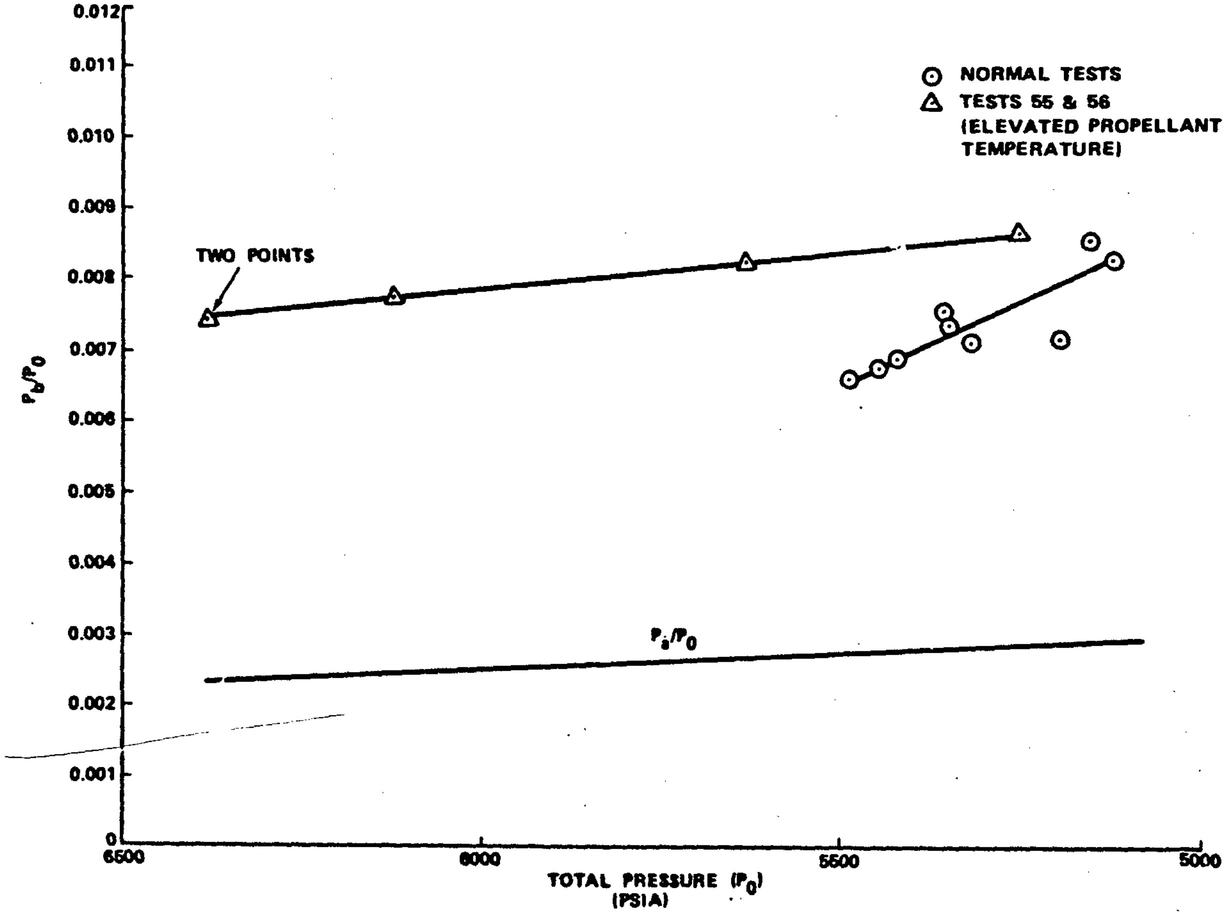

Figure 18. Base Pressures Versus Total Pressures for Hot Gas Flows

flow base bleed case by Walker [32]. The calculation method is based upon Korst's flow model. The steady-state base pressures for the cold and hot gas flows as obtained from [32] are presented in Table VI along with those obtained from experiment. Also included is the base pressure/back pressure ratio, which in this case is atmospheric pressure. Of significance is the observation that originally the base pressure was equal to the back pressure or atmospheric pressure and is increasing toward the equilibrium value. Mass is being transferred from the exhaust flow into the dead air region. In the case of the cold flow tests where the data are obtained over a much longer time

Table VI. Experimental and Predicted Base Pressure

Cold Gas			Hot Gas		
P_o (Psia)	$\frac{P_b}{P_o}$	$\frac{P_b}{P_a}$	P_o (Psia)	$\frac{P_b}{P_o}$	$\frac{P_b}{P_a}$
	Steady-State Predicted Base Pressures [32]				
NA	$\boxed{.0244}$	NA	NA	.118	NA
	Experimental Base Pressures				
2300	.0218	3.41	5440	.0066	2.44
2000	.0225	3.06	5350	.0073	2.66
1700	.0231	2.67	5135	.0082	2.86
1500	.0239	2.44			
1300	$\boxed{.0244}$	2.16			

NA - Not Applicable

span and where the total pressure is not varying as markedly as in the hot flow tests, the experimental base pressure does reach the predicted equilibrium value [32]. It is concluded that the base pressure depends on the total pressure history and that the resultant flow is dependent upon the base pressure/total pressure ratio. This conclusion is only relevant for the cold gas flows over the total pressure range which are void of the unsteady pressure waves and for the hot gas flows over the rocket motor operating chamber pressures. The flows within the tube can be treated as steady with the base pressure being a function of time. If the total pressure history is known, the base pressure variation may be determined from a quasi-steady method similar to reference [30].

Flow Symmetry, Flow Reproducibility, and Tube Length Effects

To obtain a measure of flow symmetry, three static pressure orifices were positioned 120-degrees apart around the circumference of each tube. The symmetry is determined by an evaluation of the uniformity of the static pressures sensed around the tube. The locations of these orifices in each tube are shown in Figure 11. For tubes 3 through 7, the axial location was the same. The percent variation for these three wall static pressures for a particular total pressure and for a particular experiment was determined by subtracting the smallest value from the largest and dividing by the average of the three values. For the cold and hot gas tests, this was done at each of the five total pressures. The maximum and minimum variations were noted and the average was calculated for each tube. These variations are presented in Table VII.

Table VII. Determination of the Symmetry of the Flow Using Circumferential Pressure Distribution over the Range of Stagnation Pressure

Location from Nozzle $\left(\frac{z - z_e}{r_e}\right)$	Tube	Wall Static Pressure Variation		
		Maximum (percent)	Average (percent)	Minimum (percent)
		Cold Gas		
0.22	1	3.6	2.9	1.7
2.42	2	6.4	4.1	2.1
4.82	3	6.7	4.5	2.1
4.82	4	5.9	3.2	0.5
4.82	5	9.7	5.5	1.1
4.82	6	6.3	4.5	0.1
		Hot Gas		
1.2*	1	3.1	1.6	0.4
1.2**	1	7.7	5.6	3.1
4.76	4	3.9	2.4	0.8
4.78	7	11.1	8.0	4.6

*Nominal position.
**These variations are for high temperature rocket experiments.

The inherent error of the static pressure measurement system for the cold gas experiments is ±3-1/2 percent. This error represents a maximum variation of 7 percent. All the variations for the cold gas flows except for tube 5 are within this range. For the hot gas experiments, the variations found for tube 7 exceed the predicted variation of 10 percent due to the measurement system. Under these conditions, it is difficult to distinguish the measurement error from an indication of unsymmetric flow. A marked variation in the static pressures measured at the three circumferential locations was noted at total pressures on the order of 300 to 400 psia or less in the cold gas experiments. The indicated total pressure range provided nozzle exit pressures which were approximately equal to the atmospheric pressure. It is, therefore, reasoned that these conditions are those described by Fabri and Seistrunck, corresponding to the mixed flow regime where the jet attaches to one portion of the tube wall.

Of particular interest in determining the reproducibility of the flow in the tubes are the variations of the wall static pressures from experiment to experiment. These variations are presented in Table VIII.a along with the average static pressure/total pressure ratios for the circumferential locations. Because of the small number of tests conducted for the hot gas experiments such variations would not have significance and only values are shown. The fact that the variations are relatively small for each tube indicates that the flow was reproducible in the cold gas experiments.

Also included in Table VIII.b are the effects of tube length on the static wall pressures at the circumferential location. In the case of the cold flow experiments, the average value and variations of static pressures for tubes with the same location are provided, i.e., pressures for tubes 3 through 6 with the sensor located at the axial position $(z - z_e)/r_e = 4.82$. The large variation is a result of the static pressures recorded for tube 5 as evidenced by the variation with this static pressure excluded, i.e., tubes 3, 4, and 6. The reason for the variation caused by tube 5 is unexplained. The variations for the

Table VIII-a. Variations of Static Pressure From Test to Test

Location $\left(\frac{z - z_e}{r_e}\right)$	Tube	2300 $\frac{P_w}{P_0}$	2300 Variation (Percent)	2000 $\frac{P_w}{P_0}$	2000 Variation (Percent)	1700 $\frac{P_w}{P_0}$	1700 Variation (Percent)	1500 $\frac{P_w}{P_0}$	1500 Variation (Percent)	1300 $\frac{P_w}{P_0}$	1300 Variation (Percent)
Cold Gas											
0.22	1	0.0575	1.6	0.0573	0.9	0.0567	1.2	0.0564	1.1	0.0564	1.4
2.42	2	0.0343	0.3	0.0340	2.4	0.0340	2.1	0.0339	2.1	0.0337	3.9
4.82	3	0.0188	2.7	0.0189	2.1	0.0194	1.0	0.0199	2.0	0.0204	1.0
4.82	4	0.0187	0.5	0.0189	1.6	0.0196	0.5	0.0202	3.5	0.0205	3.9
4.82	5	0.0177	1.7	0.0177	2.3	0.0181	2.2	0.0185	0.0	0.0194	1.5
4.82	6	0.0188	1.6	0.0186	1.6	0.0191	1.6	0.0198	1.0	0.0201	1.0
Hot Gas											
		5440 ±40*		5330 ±20*		5135 ±55*		6380*+		5240*+	
1.15	1	0.0226	-	0.0232	-	0.0246	-	-	-	-	-
1.27	1	-	-	-	-	-	-	0.0196	-	0.0199	-
1.39	1	0.0226	-	0.0228	-	0.0223	-	0.0221	-	-	-
4.76	4	0.0120	-	0.0124	-	0.0129	-	-	-	-	-
4.78	7	0.0117	-	0.0121	-	0.0130	-	-	-	-	-

Table VIII-b. Tube Length Effects

Cold Gas											
4.82	3,4,6	0.0188	0.5	0.0188	1.6	0.0194	2.6	0.0200	2.0	0.0204	2.0
4.82	3,4,5,6	0.0185	6.0	0.0185	6.5	0.0191	6.5	0.0196	8.7	0.0201	5.5
Hot Gas											
1.2**	1	0.0226	0	0.0230	1.7	0.0240	5.4	0.0209	12.0	-	-
4.8**	4,7	0.0119	2.5	0.0123	2.4	0.0130	0.8	-	-	-	-

* Total Pressure (psi)

** Nominal values

+ Values are for high temperature rocket experiments.

hot flow experiments are acceptable with the exception of the tests for which the rocket motor grains were at the elevated temperature prior to ignition.

Because of the limited number of pressure sensors used for each tube, a clear representation of wall static pressure distribution could not be obtained by plotting the pressure data versus positions for each individual tube. The data would be too sparse, and consequently the slope of the data curve at the points would not be determinable. To fill in the gaps and thus remedy this situation, the data obtained for each tube has to be superimposed on the same plot. This can be done only if the flow is not affected by the length of the tube, i.e., independent of tube length. In the case of fully developed supersonic flow in relatively short tubes, the flow should be independent of downstream effects, including tube length variations. The only available path for the downstream conditions to be transmitted upstream in this type of flow is through the subsonic portion of the tube wall boundary layer.

Because it is not feasible to plot and to identify every pressure measurement on one graph, the nondimensionalized static pressure data obtained at a particular location were averaged over all runs for the tube. In the case of the cold gas experiments, this was done for total pressures of 2300, 1700, and 1300 psia. These pressure distributions are presented in Figure 19. The fact that dimensionless wall static pressures at a given percentage of the tube length with different tubes are about the same verifies that the flow is independent of tube length. This is also the case for dimensionless wall

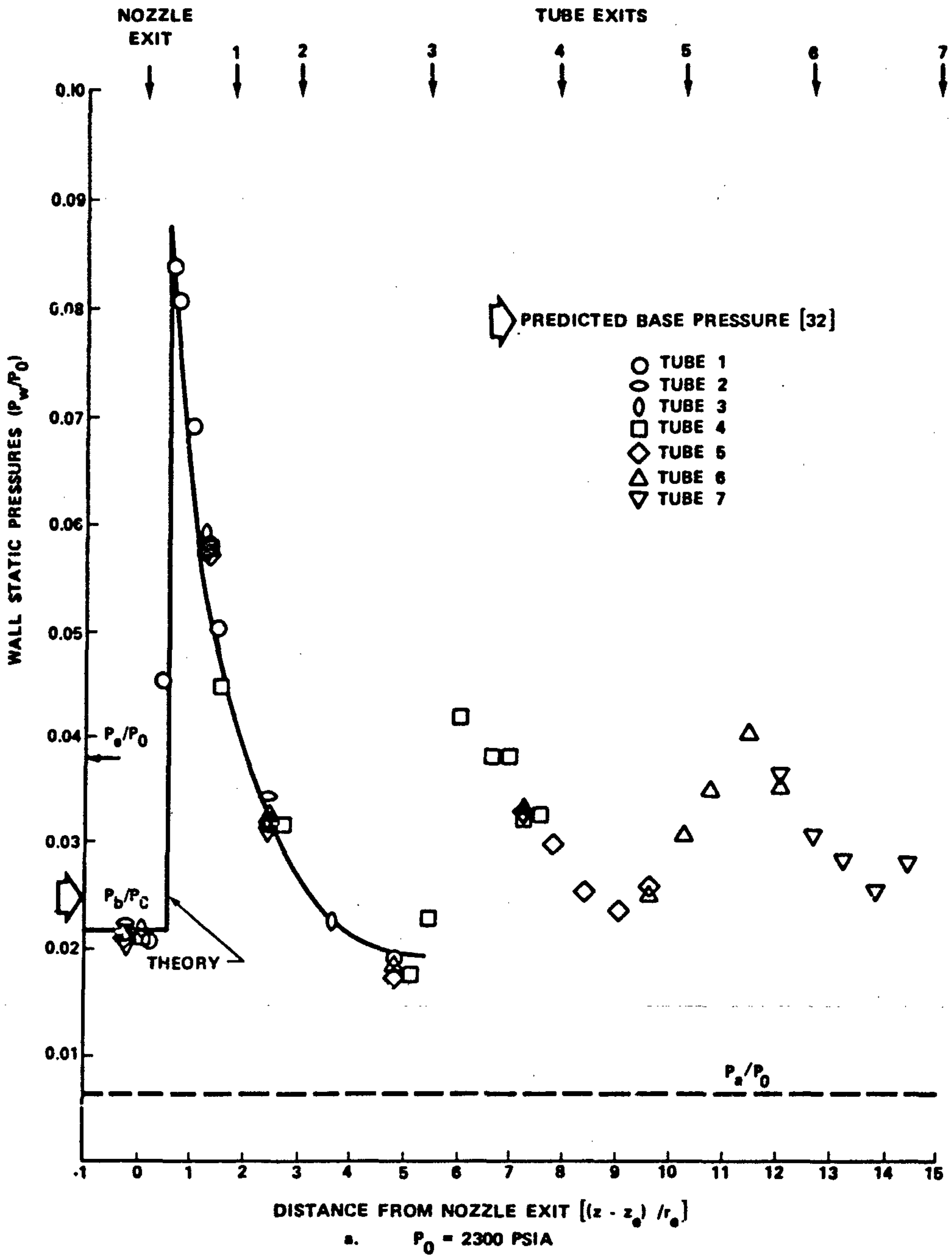

Figure 19. Wall Static Pressure Distribution

for Cold Gas Experiment, $\gamma = 1.4$

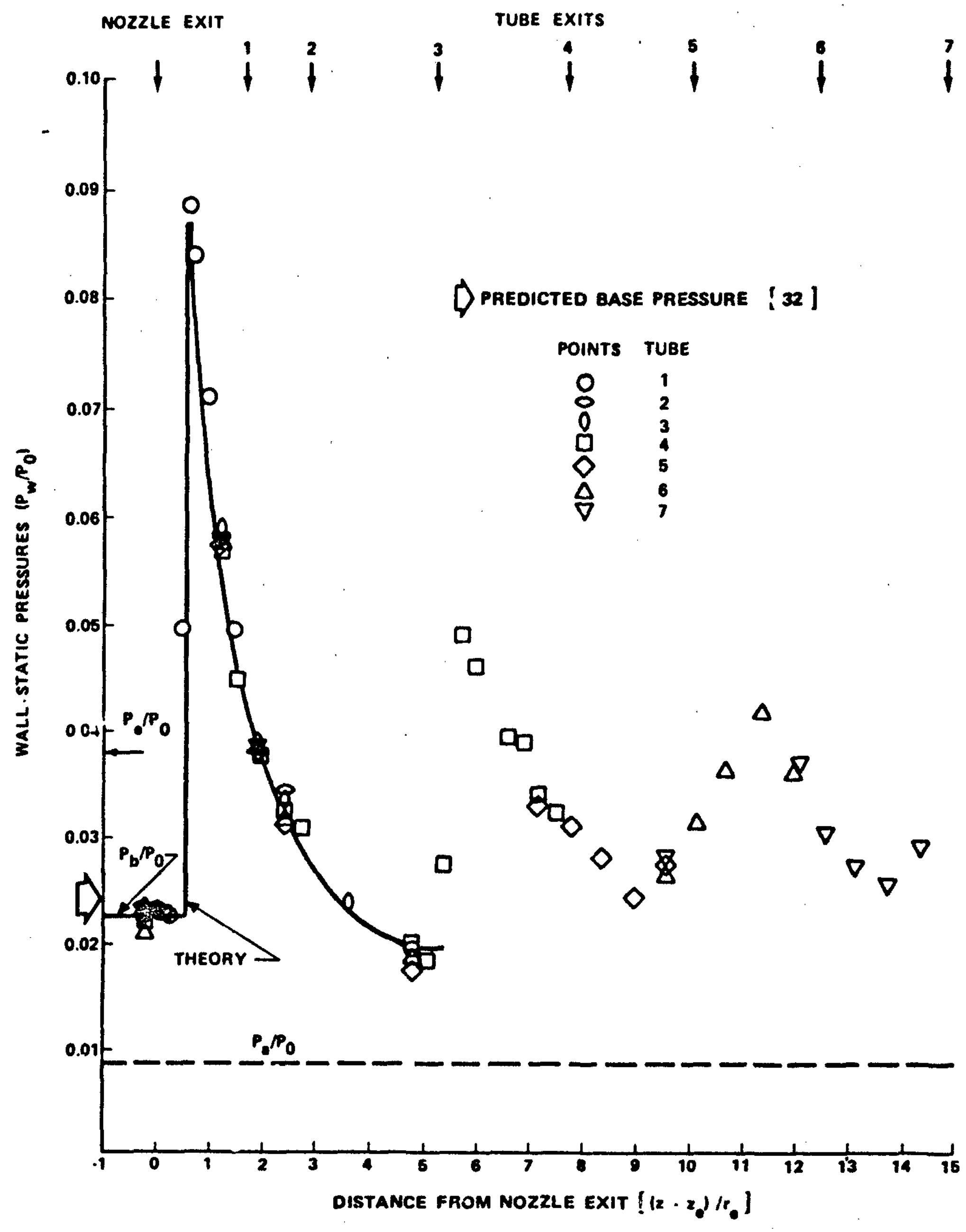

b. P_0 = 1700 PSIA

Figure 19. Wall Static Pressure Distribution

for Cold Gas Experiment, $\gamma = 1.4$ (Continued)

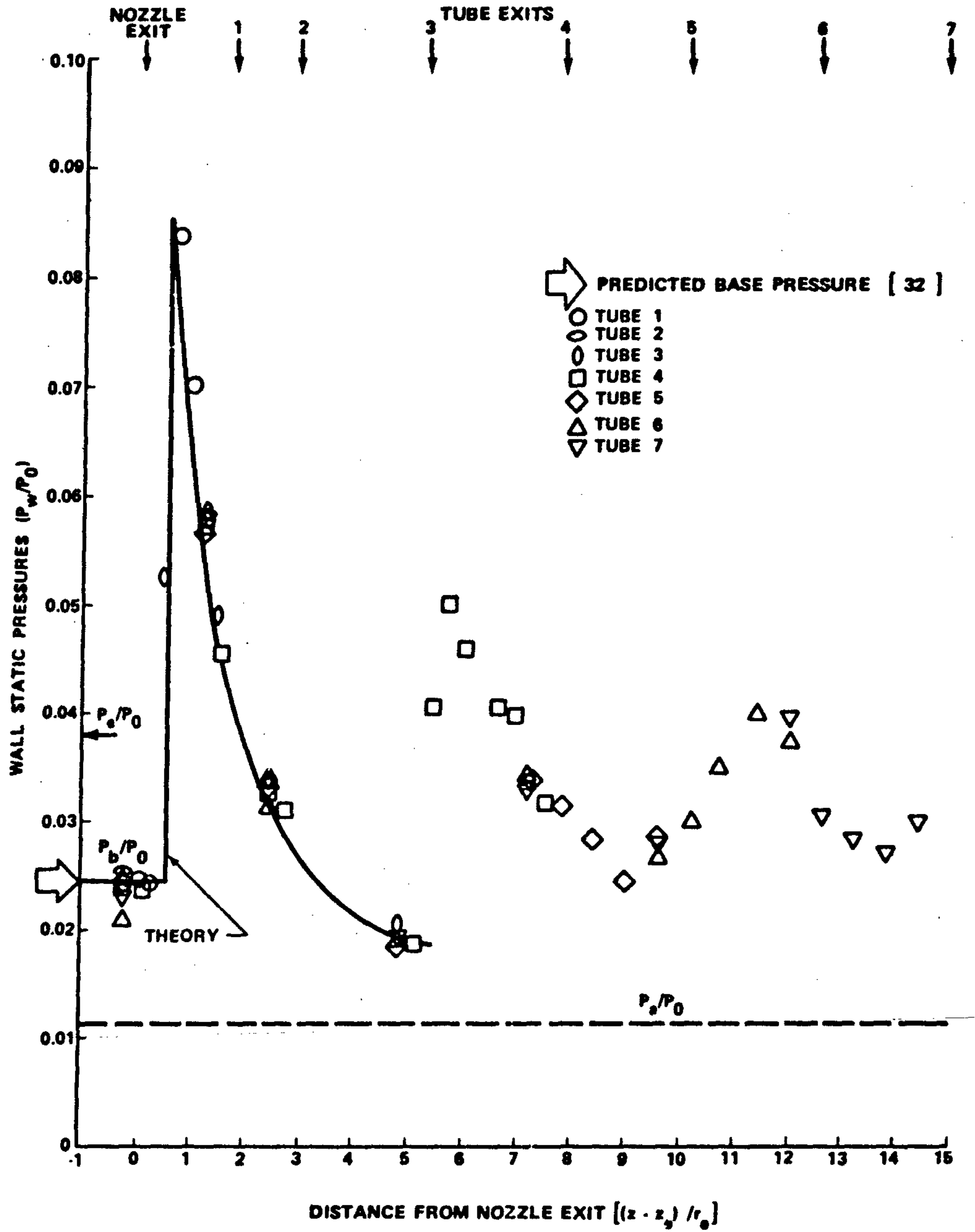

Figure 19. Wall Static Pressure Distribution for Cold Gas Experiment, γ = 1.4 (Concluded)

static pressures obtained in the hot gas experiments. These distributions for nominal total pressures of 5440, 5350, and 5135 psia, are shown in Figure 20. These nominal total pressures represent the range of motor chamber operating pressures whereas the plus or minus values shown in Figure 20 represent the range for which the static pressures were determined. Because of the short time span, the averaging method which was used for the cold gas data was not used for the hot gas data. The lack of data oints in this figure and the incompleteness of the curve are a result of the small number of hot gas experiments which were conducted. The observation that the flow is independent of tube length is in consonance with that of German et al. [15] which was also empirically determined and that of Fabri and Siestrunck [3] which was ascertained by theory. The reproducibility of flow from test to test is also indicated by the relatively small scatter in the data of Figures 19 and 20.

Wall Static Pressure Distribution

The flow exiting the tubes was fully developed supersonic in nature as evidenced by the shock wave and expansion waves which were created by the presence of the pitot rake in the flow. This information was visible on the 16-mm and 70-mm films. Thus it is concluded that the flow was supersonic throughout the tube.

The analytical flow model with its inherent assumptions was closely approximated in the experimental investigation. To obtain a correlation of theory with the results of the experimental investigation, the experimental base pressures together with the experimental

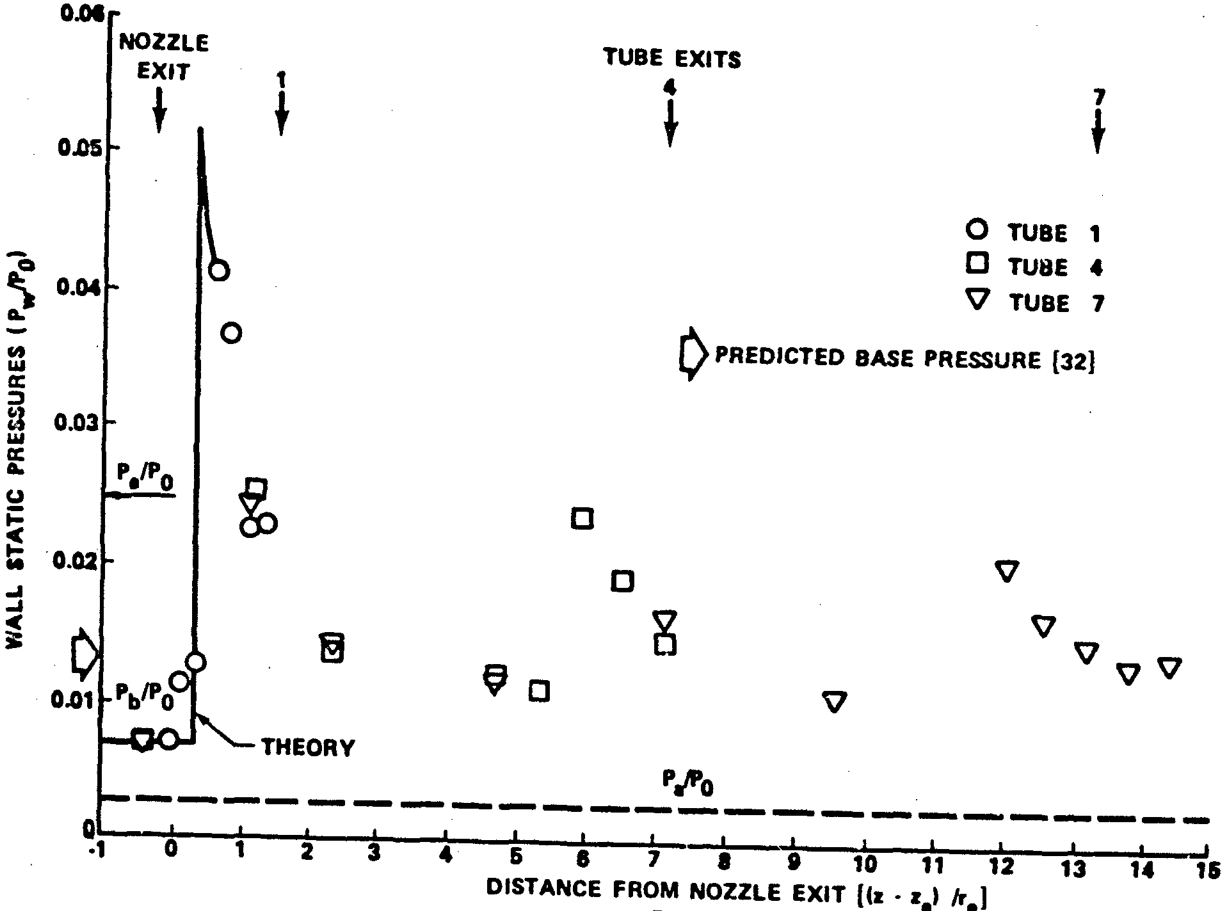

a. 5440 ± 40 PSIA

Figure 20. Wall Static Pressure Distribution for Hot Gas Experiments, γ = 1.23

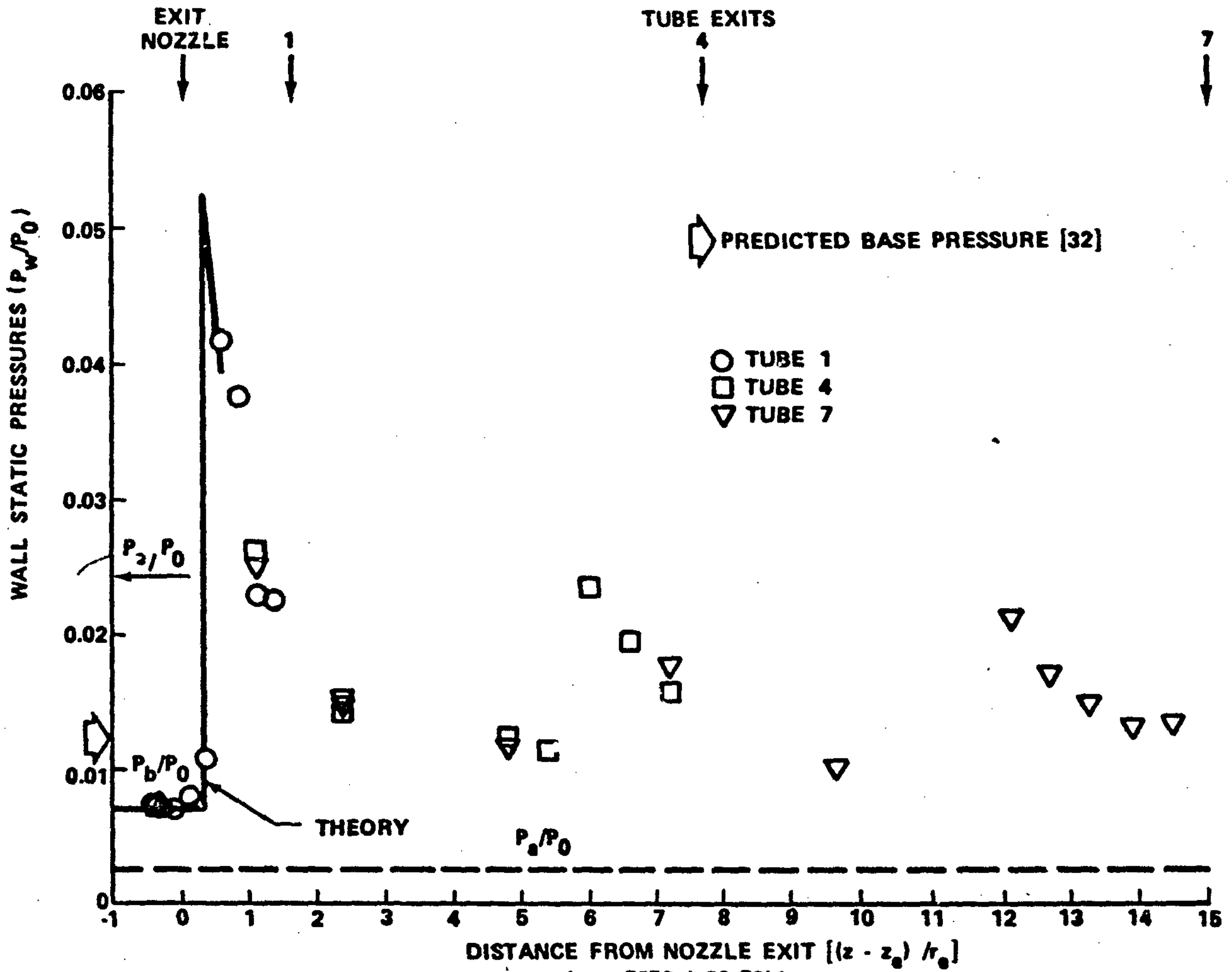

b. 5350 ± 20 PSIA

Figure 20. Wall Static Pressure Distribution for Hot Gas Experiments, $\gamma = 1.23$ (Continued)

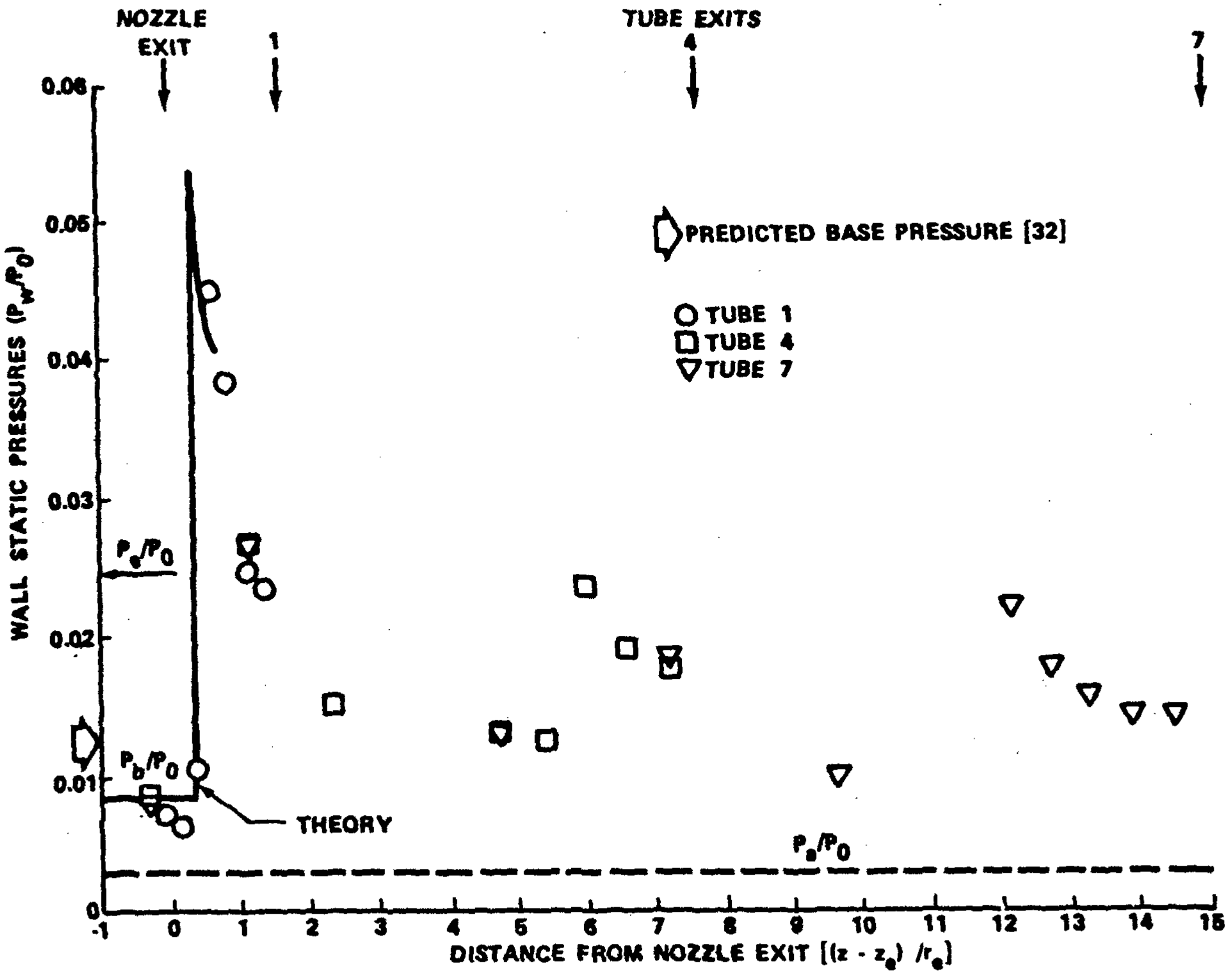

c. P_0 = 5135 ± 55 PSIA

Figure 20. Wall Static Pressure Distribution for Hot Gas Experiments, γ = 1.23 (Concluded)

geometric constraints and the ratio of specific heats were used as inputs to the theoretical computer program for the theoretical analysis. This was done for the hot and the cold flows. The predicted wall static pressure distributions are superimposed on the experimental data in Figures 19 and 20. As can be seen, the theoretical analysis adequately defines the first pressure peak. The predicted pressure data are satisfactory, indicating the approximation method used in the theoretical analysis is satisfactory with respect to defining the pressure variations. The approximate theory developed herein cannot define the second or third peaks. The nozzle exhaust expands to the base pressure and the jet boundary-wall intersection position is a function of this pressure. The pressures along the wall behind the impingement shock are governed by the base pressure, since it dictates the shock strength, in essence, by dictating the jet-boundary Mach number and flow angle. For fully developed supersonic flow in the tube, it is reasonable to expect that a change in base pressure will cause the pressures along the wall or the flow pattern in the tube to change. However, note from Figures 19 and 20 that there is a distinct variation in base pressure with respect to total pressure, whereas the static pressure distribution along the wall appears to change only slightly with a total pressure change. As expected, the maximum wall static pressure occurs just downstream of the impingement shock-wall intersection for both the cold and the hot gas flows (Figures 19 and 20). The maximum wall static pressures obtained from theory agree with those found by experiment. The theoretical maximum wall pressure for each base pressure obtained by experiment and obtained from reference [32] is listed in Table IX.

Table IX. Maximum Predicted Wall Static Pressure

Cold Gas			Hot Gas		
P_0 (Psia)	$\frac{P_b}{P_0}$	$\frac{P_{w\,max}}{P_0}$	P_0 (Psia)	$\frac{P_b}{P_0}$	$\frac{P_{w\,max}}{P_0}$
2300	0.0218	0.0870	5440	0.0066	0.0517
2000	0.0225	0.0865	5350	0.0073	0.0526
1700	0.0231	0.0861	5135	0.0082	0.0535
1500	0.0239	0.0854			
1300	0.0244 *	0.0850		0.0118 *	0.0542

* Predicted base pressure [32]

Because the maximum wall pressure varies slightly with base pressure, an adequate estimate of this pressure can be obtained for engineering purposes by using the steady-state base pressure as predicted by reference [32]. At no time during the experimental runs did the absolute value of the maximum wall pressure exceed that obtained at the maximum total pressure during the run. Thus, it can be concluded that maximum wall pressure occurs at the same time as the maximum total pressure.

Supersonic Flow Pattern in the Tube

A further characterization of the flow within the tube hinges on the correlation between the wall static pressures and the photographic evidence. According to Fabri (Figure 2.c), the three static pressure peaks, which are evident in Figures 19 and 20, are caused by oblique shocks intersecting the wall. The shock pattern within the tube, as deduced from these pressure peaks, and the shock locations, as manifested in the 70-mm photographs of the flow exiting the tube, are shown in Figure 21. The impingement shock which causes the first pressure peak is evident in the 70-mm photographs of the flow exiting from tubes 1 and 2 (Figures 22 and 23).

The impingement shock causes the flow in the jet boundary to turn and proceed along the tube wall. This shock emanates from the jet boundary-wall intersection and projects to the tube axis as an apparent paraboloid surface. The time and, consequently, the total pressure conditions for the flows shown in these photographs are unknown. They are not shadowgraphs or schlieren, although a high intensity lamp was used for lighting. The process which makes the flow visible is the scattering of light from the vapor condensed in the flow itself as it expands or on the flow boundary, in which case, the condensed vapor was entrained from the atmosphere. The shock processes the flow (i.e., increases the temperature and pressure), thus vaporizing the condensation so that the shock location can be identified. This photographic technique also can picture large density gradients (such as a shadowgraph) as evidenced in some photos which show the shocks that develop because of the pitot probes. The impingement shock intersects the nozzle axis just aft of tube 2. This intersection point is indicated on the ordinate in Figure 21.

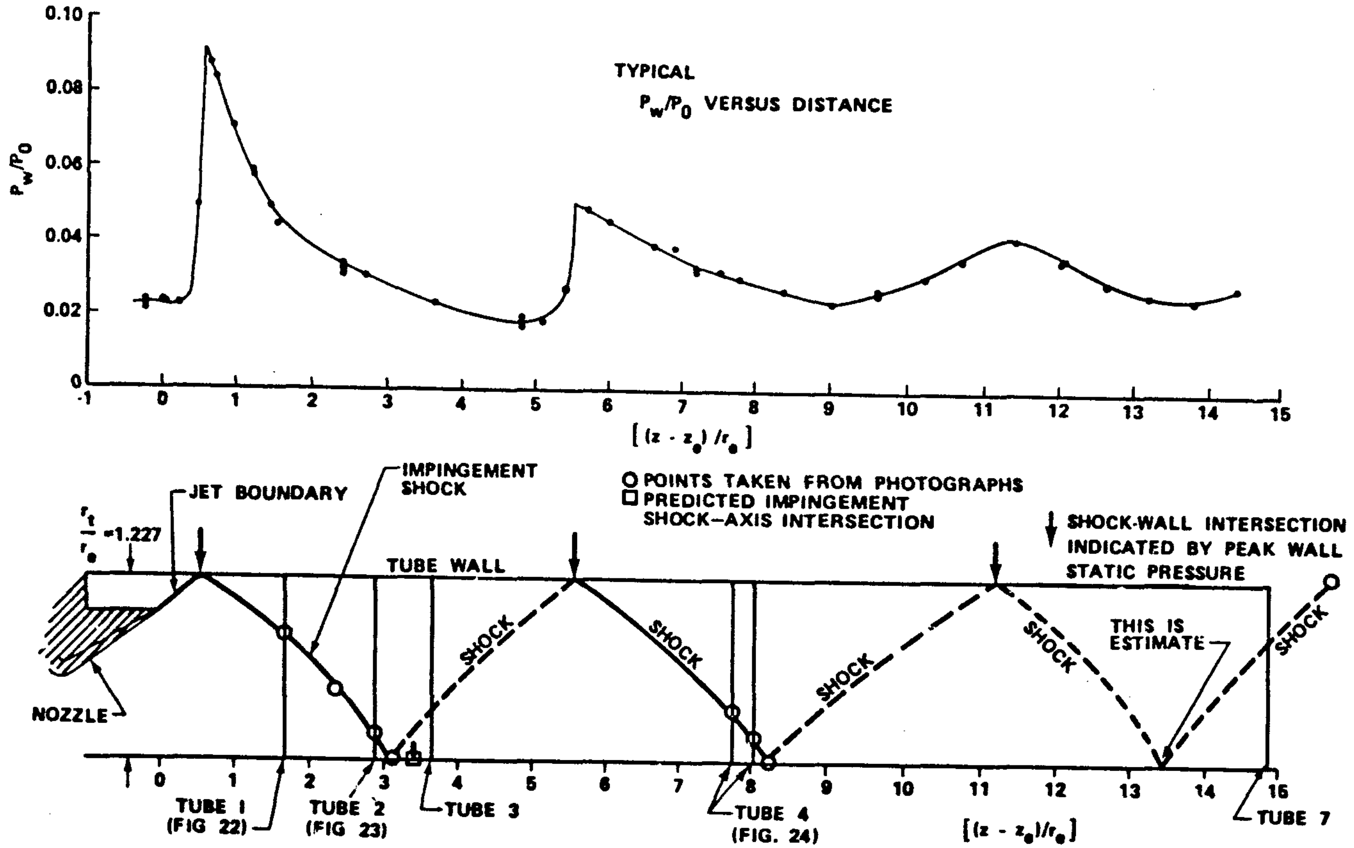

Figure 21. Impingement Shock-Axis Location

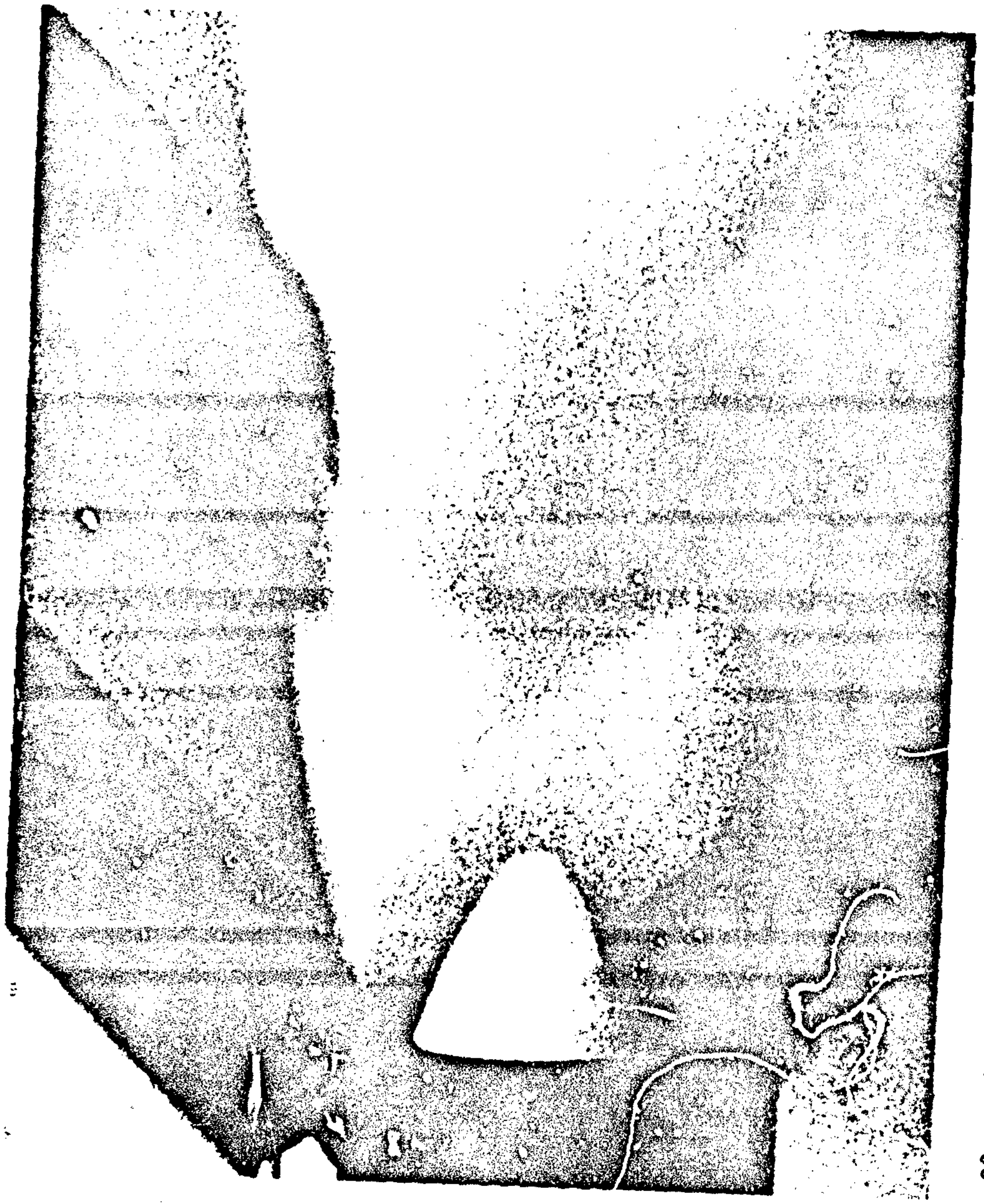

Figure 22. Cold Flow Exiting Tube 1 (Shows Impingement Shock Intersecting the Tube Axis)

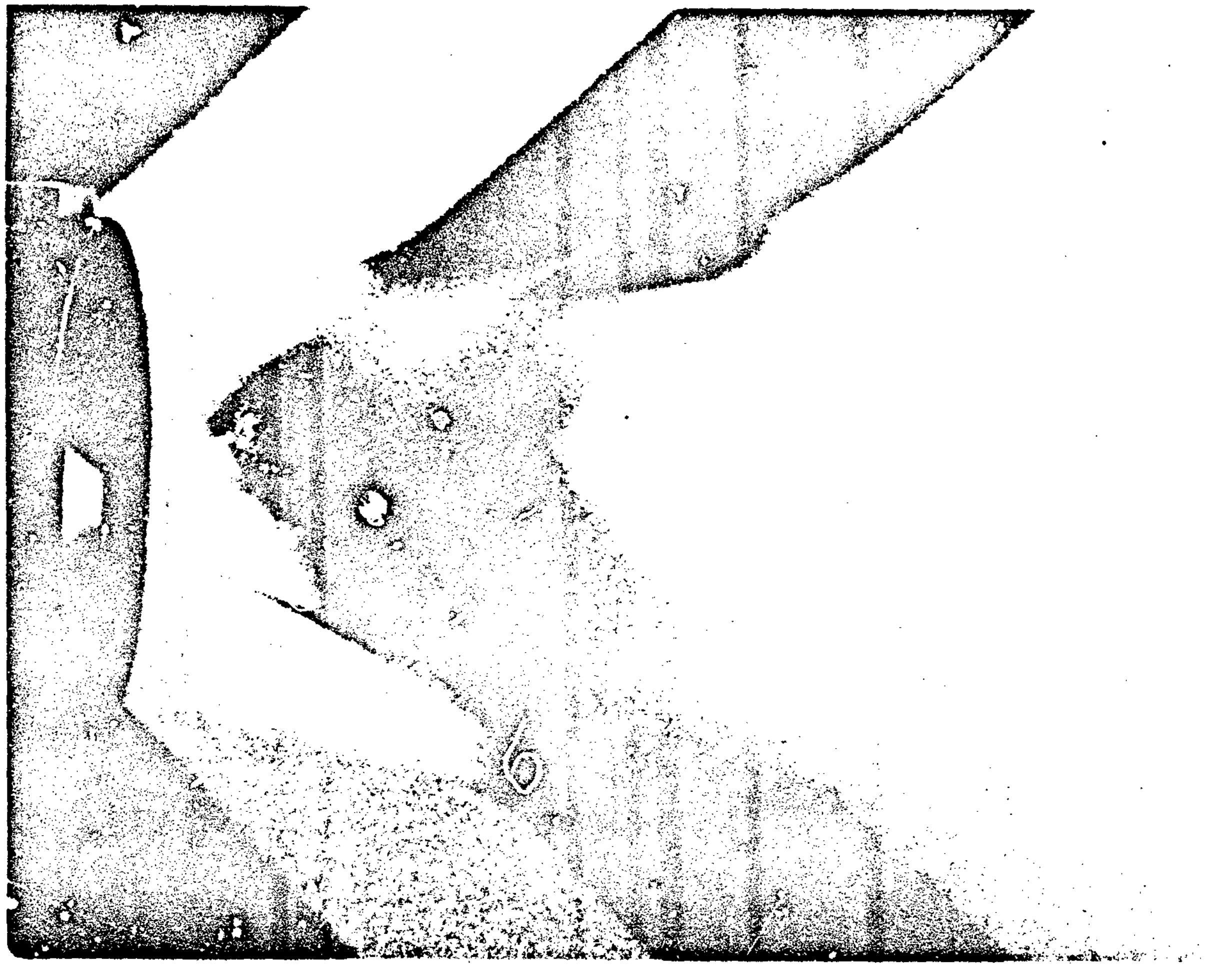

Figure 23. Cold Flow Exiting Tube 2 (Shows Impingement Shock Intersecting the Tube Axis)

Also shown in this figure is the impingement shock-axis location as predicted by the theoretical analysis. The theory gives a good indication of this point. However, it should be noted, that in order to obtain this point by the described theoretical method, the shock has to be projected theoretically to the axis. The theoretical approach is not expected to be accurate at the axis. Descriptions of the flow field as obtained from the analytical investigation of the cold and hot gas flows are presented in Appendix C. The second pressure peak is attributed to the impingement shock reflecting from the axis back to the wall. This is not apparent in the photograph of the flow exiting tube 3.

Figure 24 shows the shock projecting from the point on the wall, which corresponds to the second pressure peak, to the axis. This photograph was taken at the exit of tube 4. The tube was moved aft 0.263 inch in Figure 24.b. The shock-axis intersection point is indicated on Figure 21. Both shock-axis intersection points (impingement shock and second shock) occur when the tube wall static pressures were decreasing to their minimums.

The exit planes of tubes 3, 5, and 7 are near the three valleys for the wall static pressure and should give an indication of the shocks reflecting from the tube axis. No shocks were evident; however, a bulge or an expansion in the tube exhaust flow did occur downstream of the tube exit. As it exits from the tube, the flow expands very little denoting that the tube exit pressure is slightly larger than atmospheric. At a finite distance downstream, the flow expands radically indicating a considerable increase in pressure

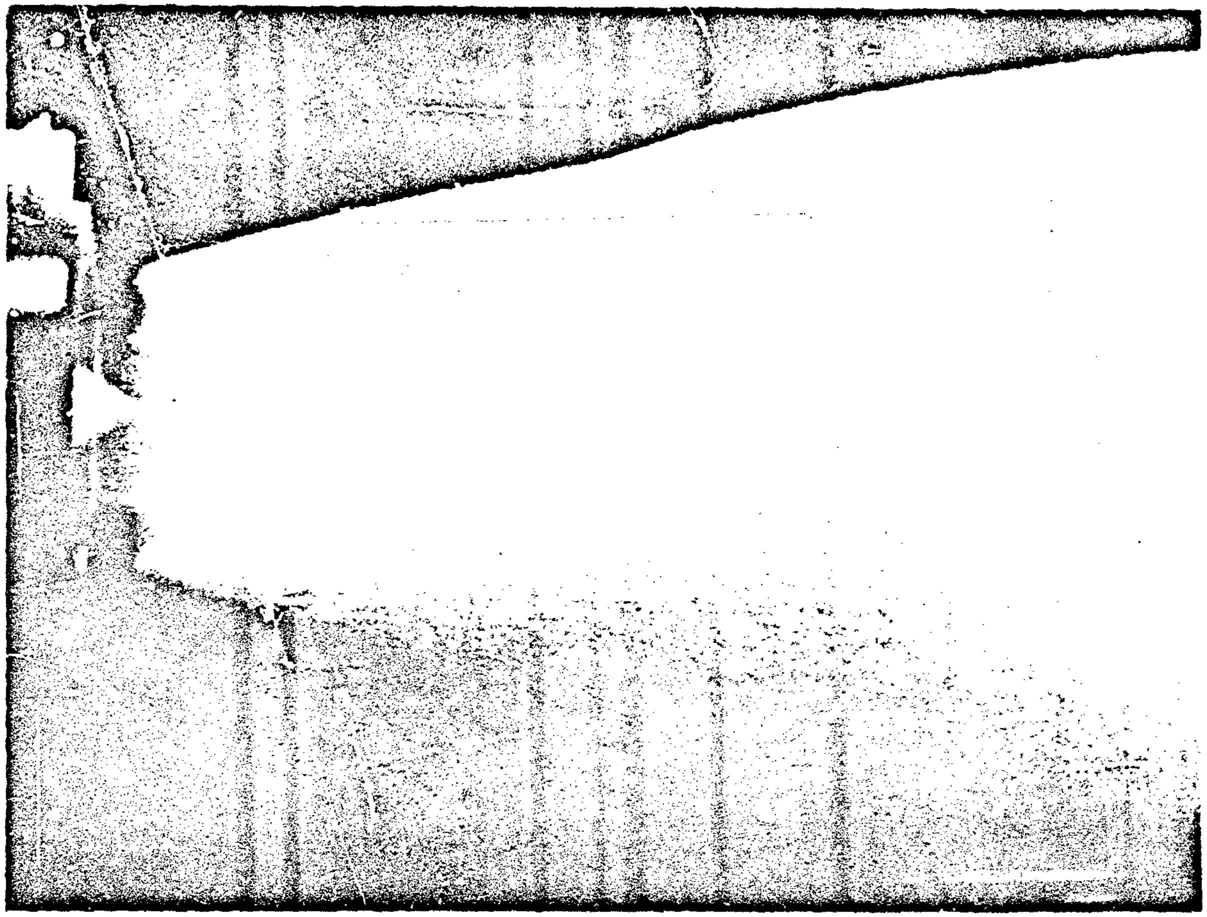

TUBE IN NORMAL POSITION

Figure 24.a. Cold Flow Exiting Tube 4 (Shows Second Shock Intersecting the Tube Axis)

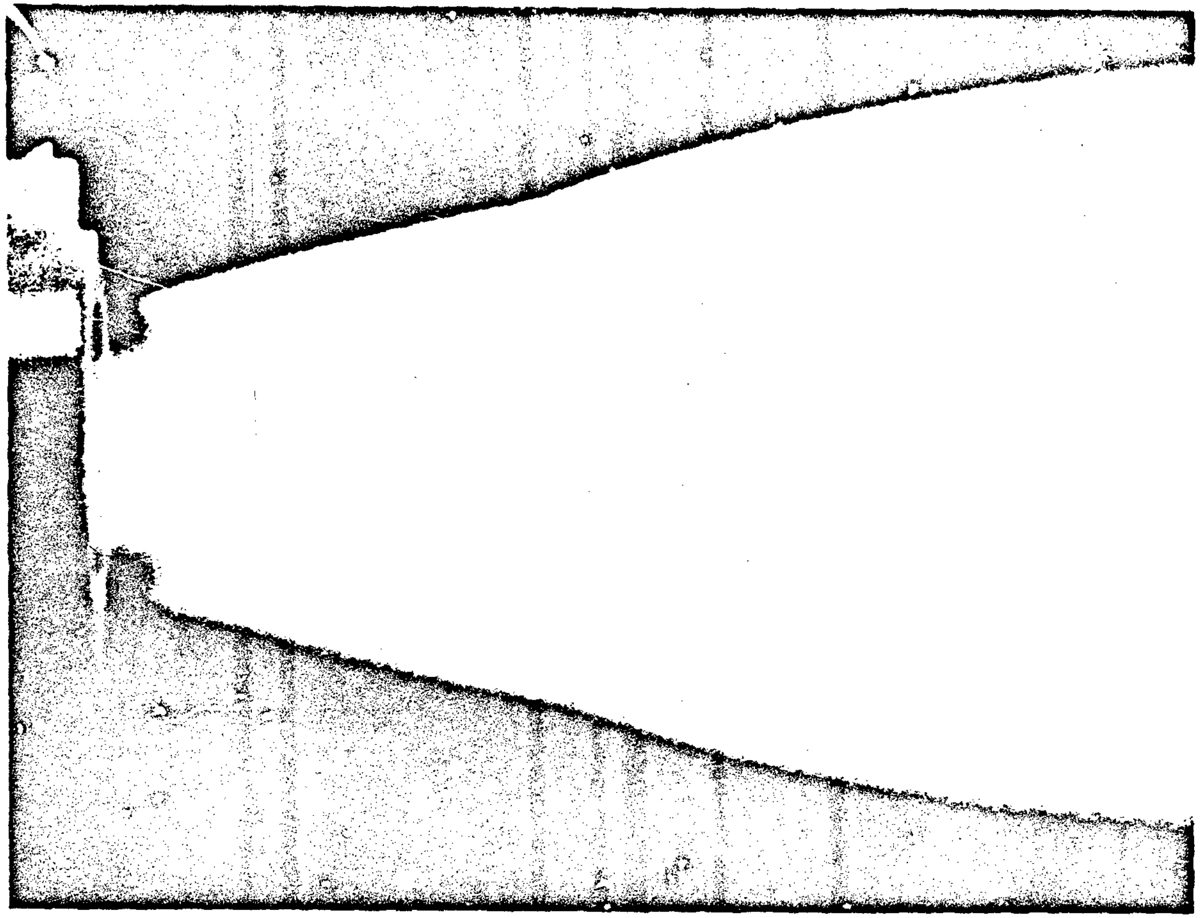
TUBE MOVED AFT 0.263 INCH

Figure 24.b. Cold Flow Exiting Tube 4 (Shows Second Shock Intersecting the Tube Axis)

which could be caused by the shock. The point outside of tube 7 in Figure 21 was obtained from this bulge. The shock emanating from the wall at the third pressure peak is not evident in the photograph of the flow exiting tube 6.

The cold flow is supersonic throughout the tubes. The flow patterns give further evidence that the flow is axially symmetric. The correlation of the pitot data, which were obtained at different radial locations in the flow, with theory in the conical region and the analysis of the circumferential wall static pressures also verifies that the flow is axially symmetric. The anomaly found in the evaluation of the circumferential static pressures for tube 5 has not been resolved and is attributed to instrument error. The 16-mm movie coverage of the hot gas experiments also revealed that the flows within the tube were supersonic and symmetric.

CHAPTER VI

CONCLUDING REMARKS

The present investigation was undertaken to develop a design model for the flow field which results when an underexpanded rocket exhaust exits from a conical nozzle into a cylindrical tube. The experimental phase of the investigation employed short duration cold gas flows and actual rocket exhausts. The reservoir pressure to back pressure relation was large, as high as 350, and was not constant but varied markedly with time during an experiment. The resulting nozzle exit pressure/back pressure ratio varied from 9.2 to 3.4. The tube configurations considered consisted of relatively short cylindrical tubes, less than 6.2 tube internal diameters long, with a tube radius to nozzle exit radius, r_t/r_e of 1.2. The analytical phase of the study sought to verify the empirical flow model. Based on the data obtained in the present study the following conclusions were made about the flow field in the cylindrical tube:

(1) The nozzle exhaust flow along the entire length of the tube is supersonic with the wall static pressures being greater than the atmospheric back pressure. The base pressure is less than the nozzle exit pressure indicating that underexpanded nozzle flow exists.

(2) The base pressure/reservoir pressure relation is not constant but varies for fully developed supersonic flow as the reservoir pressure varies. The ratio of base

pressure/reservoir pressure approaches the predicted static equilibrium value. The base pressure depends on the reservoir pressure and the resultant flow field characteristics in the tube are dependent upon the base pressure/reservoir pressure ratio.

(3) The wall pressure measurements indicate an abrupt pressure rise downstream of the first impingement shock. For the conditions considered, the viscous effects have little apparent influence on the impingement shock structure other than the effects on base pressure.

(4) The flow in the tube is independent of tube length.

(5) After the base pressure is determined from an existing theory, the location of the first impingement shock and the wall pressure distribution in the vicinity of the shock wave can be calculated analytically.

(6) The wall pressure peak occurs immediately downstream of the first impingement shock and is greatest when the reservoir pressure is the greatest. Thus, the critical stress for the tube design can be readily calculated.

APPENDIX A

FINITE DIFFERENCE EQUATIONS FOR STEADY, AXISYMMETRIC, POTENTIAL FLOW AND STEADY, AXISYMMETRIC, ROTATION FLOW

Equations of Characteristics

The following equation is valid for steady, axisymmetric, potential flow:

$$\cot \mu \frac{dq}{q} \mp d\theta - \frac{\sin \mu \sin \theta}{\cos(\theta \pm \mu)} \frac{dz}{r} = 0 \quad . \qquad \text{(A-1)}$$

For steady, axisymmetric, rotational flow, the following equation is valid:

$$\cot \mu \frac{dq}{q} \mp d\theta - \frac{\sin \mu \sin \theta}{\cos(\theta \pm \mu)} \frac{dz}{r} + \sin \mu \cos \mu \frac{dS}{\gamma \mathcal{R}} = 0 \quad . \qquad \text{(A-2)}$$

Along physical characteristics lines

$$\frac{dr}{dz} = \tan (\theta \pm \mu) \qquad \text{(A-3)}$$

and

$$dS = 0$$

Along the streamline defined by

$$\frac{dr}{dz} = \tan \theta \qquad \text{(A-4)}$$

The previously mentioned equations are derived in and are taken from Ferri [26].

By substituting Equation (A-3) and the Prandtl-Meyer function $d\upsilon = \cot\mu \frac{dq}{q}$ into Equations (A-1) and (A-2):

$$d(\upsilon \mp \theta) - \frac{\sin\mu \sin\theta}{\sin(\theta \pm \mu)} \frac{dr}{r} = 0 \tag{A-5}$$

$$d(\upsilon \mp \theta) - \frac{\sin\mu \sin\theta}{\sin(\theta \pm \mu)} \frac{dr}{r} + \sin\mu \cos\mu \frac{dS}{\gamma\mathcal{R}} = 0 \quad . \tag{A-6}$$

Since

$$\sin(\theta \pm \mu) = \sin\theta \cos\mu \pm \cos\theta \sin\mu \quad ,$$

and $\frac{\sin\mu \cos\theta}{\sin(\theta \pm \mu)}$ becomes $\frac{1}{\cot\mu \pm \cot\theta}$,

Equation (A-5) becomes

$$d(\nu \mp \theta) = \frac{1}{\cot\mu \pm \cot\theta} \frac{dr}{r} \quad , \tag{A-7}$$

and Equation (A-6) becomes

$$d(\nu + \theta) = \frac{1}{\cot\mu \pm \cot\theta} \frac{dr}{r} - \sin\mu \cos\mu \frac{dS}{\gamma\mathcal{R}} \tag{A-8}$$

Steady, Axisymmetric, Potential Flow

Finite Difference Equations

Points 1 and 2 in Figure A-1 are two known points at which the flow characteristics are known. The position and flow characteristics of point 3 are unknown. The position of point 3 can be obtained from Equation (A-3) in finite difference form, i.e.,

$$\frac{\Delta r}{\Delta z} = \overline{\tan(\theta \pm \mu)} \qquad \text{(A-9)}$$

where Δ denotes the variation of a property between two points and the bar denotes the average property of two points.

$$\frac{r_3 - r_2}{z_3 - z_2} = \frac{1}{2}\left[\tan(\theta + \mu)_2 + \tan(\theta + \mu)_3\right] \qquad \text{(A-10)}$$

$$\frac{r_3 - r_1}{z_3 - z_1} = \frac{1}{2}\left[\tan(\theta - \mu)_1 + \tan(\theta - \mu)_3\right] \qquad \text{(A-11)}$$

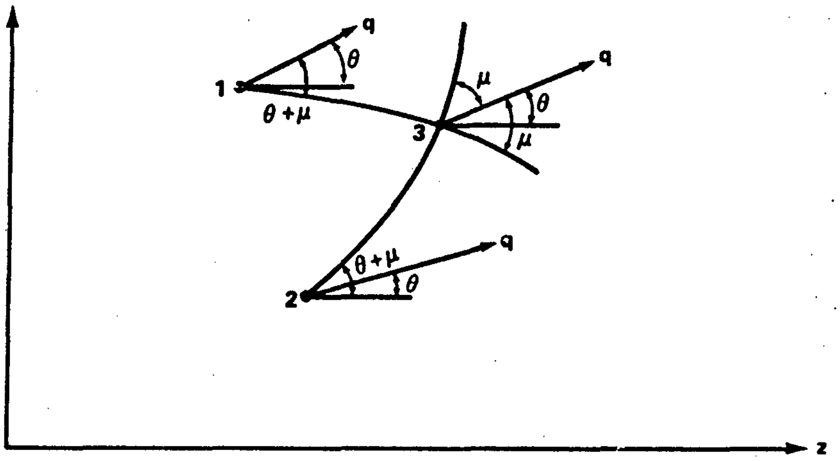

Figure A-1. Characteristics Net for an Interior Point

The flow characteristics at point 3 are obtained from Equation (A-7) by letting $\frac{1}{(\cot\mu \pm \cot\theta)}$ be equal to a constant average value, i.e., $\frac{1}{[\overline{\cot\mu \pm \cot\theta}]}$ and then integrating between two points

$$(\nu - \theta)_3 - (\nu - \theta)_2 = \frac{1}{\frac{1}{2}\left[\cot \mu_2 + \cot \theta_2 + \cot \mu_3 + \cot \theta_3\right]} \ln \frac{r_3}{r_2} \qquad \text{(A-12)}$$

and

$$(\nu + \theta)_3 - (\nu + \theta)_1 = \frac{1}{\frac{1}{2}\left[\cot \mu_1 - \cot \theta_1 + \cot \mu_3 - \cot \theta_3\right]} \ln \frac{r_3}{r_4} \quad . \qquad \text{(A-13)}$$

Equations (A-10) through (A-13) are the governing characteristics equations for steady, axisymmetric, potential flow in finite difference form. These equations are identical to those of Owczarek [24].

Steady, Axisymmetric, Rotational Flow
Finite Difference Equations

The relation for change in entropy with respect to total pressure drop is

$$\frac{dS}{\mathcal{R}} = - \frac{dP_0}{P_0} \quad . \qquad \text{(A-14)}$$

Substitute Equation (A-14) into Equation (A-6) and realize that sin 2 μ = 2 sin μ cos μ gives

$$d(\nu \mp \theta) - \frac{1}{\cot \mu \pm \cot \theta} \frac{dr}{r} - \frac{\sin 2\mu}{2\gamma} \frac{dP_0}{P_0} = 0 \quad . \qquad \text{(A-15)}$$

Note Equation (A-3) is

$$\frac{dr}{dz} = \tan(\theta \pm \mu) \qquad . \qquad \text{(A-16)}$$

Because the rotational flow equations will be used behind the shock and the values of some θ's and r's are likely to be zero, the following finite difference form will be used to facilitate numerical evaluation:

$$\Delta[\nu \mp \theta] = \frac{1}{\cot \bar{\mu} \pm \cot \bar{\theta}} \frac{\Delta r}{\bar{r}} - \frac{\sin 2\bar{\mu}}{2\gamma} \frac{\Delta P_0}{\bar{P}_0} \qquad \text{(A-17)}$$

$$\frac{\Delta r}{\Delta z} = \tan[\bar{\theta} \pm \bar{\mu}] \qquad . \qquad \text{(A-18)}$$

The finite difference form of Equations (A-17) and (A-18) are the same type as derived by Ruo [27].

Equations (A-17) and (A-18) are the governing characteristics equations for steady, axisymmetric, rotational flow in finite difference form.

APPENDIX B

DETAILED COMPUTATION METHOD FOR AXIALLY SYMMETRIC ROTATIONAL FLOW REGION BY AN APPROXIMATE FINITE DIFFERENCE METHOD OF CHARACTERISTICS

Flow Conditions Behind the Impingement Shock

The following examples of the use of the rotational flow equations are orientated to the characterization of the flow behind the impingement shock wave. In particular, these equations in conjunction with the equations for an oblique shock will be used to determine the position of the shock, the total pressure drop across the shock, the Mach number, and flow direction behind the shock [27, 28, 29]. Figure B-1 shows the angles through an oblique shock.

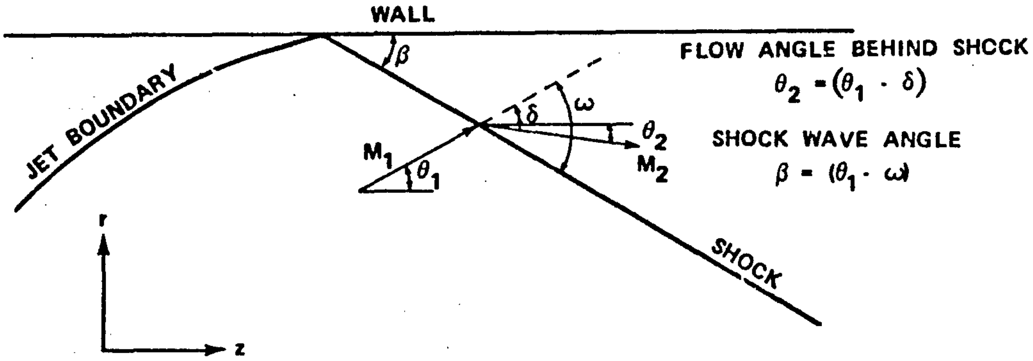
WALL
JET BOUNDARY
β
δ
ω
M_1
θ_1
θ_2
M_2
FLOW ANGLE BEHIND SHOCK
$\theta_2 = (\theta_1 - \delta)$
SHOCK WAVE ANGLE
$\beta = (\theta_1 - \omega)$
SHOCK
r
z

Figure B-1. Flow Through an Oblique Shock Wave

The conditions behind the shock at the jet boundary-wall intersection (position I in Figure B-2) and the shock angle, β, are

PRECEDING PAGE BLANK-NOT FILMED

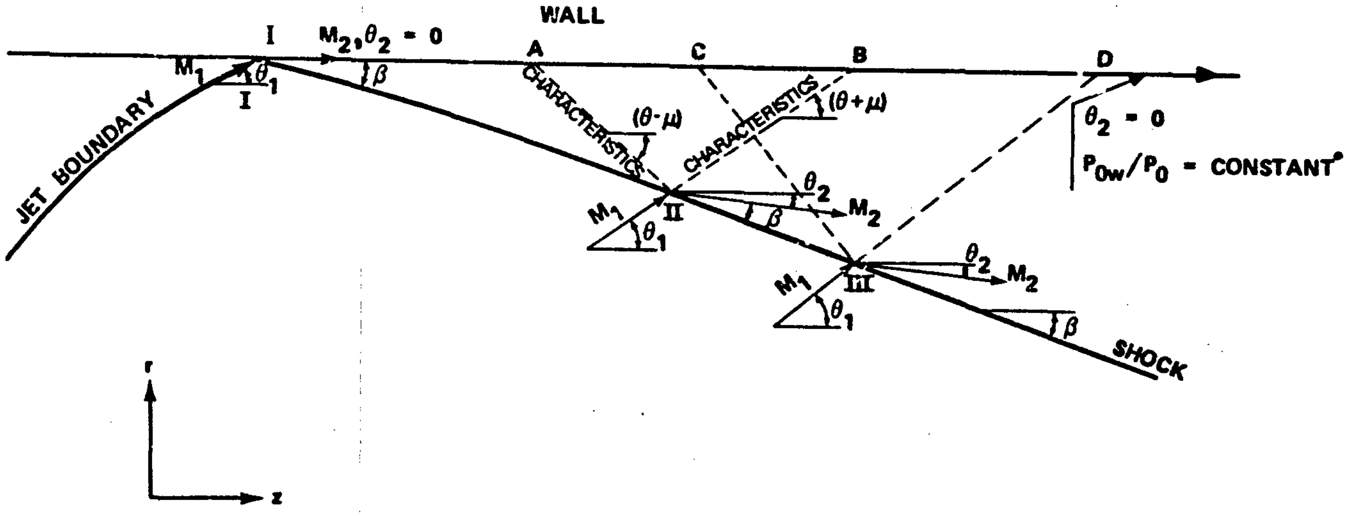
WALL
I
$M_2, \theta_2 = 0$
A
C
B
D
M_1
θ_1
I
β
JET BOUNDARY
CHARACTERISTIC
$(\theta - \mu)$
CHARACTERISTICS
$(\theta + \mu)$
$\theta_2 = 0$
P_{0w}/P_0 = CONSTANT
M_1
II
θ_1
θ_2
M_2
β
M_1
III
θ_1
θ_2
M_2
β
SHOCK
r
z

Figure B-2. Jet Boundary-Wall Intersection readily determined from the oblique shock equations, because θ_2, the flow angle behind the shock, is zero; i.e., the flow turns parallel with the tube wall.

Because the wall constitutes a streamline for inviscid flow, the angle $\theta_2 = 0$ and P_{02}/P_{01} along the wall is constant ($dS = 0$ along a streamline). However, the Mach number and, consequently, the pressure along the wall may vary.

Isentropic Flow Characteristic - Shock Wave Intersection

The procedure required to calculate the flow down stream of the shock wave at point III is typical of the procedure for points along the impingement shock but away from the wall. The position of point III can be obtained from geometry because the shock angle, β, is known at point II. Flow conditions upstream of the shock at point III are obtained from the isentropic flow solution. At point III, a problem arises because neither the Mach number nor the flow angle behind the shock is known. The oblique shock equations require that one or the other be known. A characteristics net must be constructed behind the shock and the rotational flow and oblique shock equations must be solved simultaneously. In this case, they are solved numerically by an iteration process.

Consider Figure B-2 where point III is close to the wall and the flow conditions behind the shock are unknown. For illustration, assume that the flow conditions along the wall are known as a function of z out to B. Hence, if the position of C can be determined, the flow conditions are known. Also, assume that the conditions behind the shock at point II are known.

However, the conditions behind the shock at point III are unknown. Assume that θ_2 at point III is equal to θ_2 at point II and solve the shock equations to determine the flow conditions behind the shock.

The flow conditions must also satisfy the rotational flow characteristics net behind the shock. Solve the characteristics equations along the characteristic C-III in terms of ν_{III} by the finite difference equations:

$$[\nu + \theta]_{III} - [\nu]_C = \frac{1}{\cot\left[\frac{\mu_C + \mu_{III}}{2}\right] - \cot\frac{\theta_{III}}{2}} \; \frac{\left[r_{III} - r_t\right]}{\frac{1}{2}\left[r_{III} + r_t\right]} + \frac{\sin\left[\mu_C + \mu_{III}\right]}{2} \; \frac{\left[\frac{P_{0_{III}}}{P_0} - \frac{P_{0_I}}{P_0}\right]}{\frac{1}{2}\left[\frac{P_{0_{III}}}{P_0} + \frac{P_{0_I}}{P_0}\right]} \qquad \text{(B-1)}$$

and

$$\frac{r_{III} - r_t}{z_{III} - z_C} = \tan\left[\frac{\theta_{III}}{2} - \frac{\mu_C + \mu_{III}}{2}\right] \quad . \qquad \text{(B-2)}$$

These equations cannot be solved because the characteristic-wall intersection position, z_C , is unknown. If z_C were known, the flow conditions at C would be known (based on an original assumption). For the first approximation, let the flow conditions at C equal to the flow conditions of the previous characteristic-wall intersection A, i.e., $\nu_C = \nu_A$ and $\mu_C = \mu_A$. By solving Equation (B-2), a new z-position for point C will be generated. Because the flow conditions along the wall are assumed a function of z, the flow conditions are also known. The new values are substituted into Equation (B-2). This process is repeated until $(\nu_C)_m - (\nu_C)_{(m-1)} = \varepsilon$, where ε is a small acceptable value.

Note the first approximation of ν_{III} is obtained using the Mach angle, μ_{III}, found by the oblique shock equations. The next approximation for ν_{III} is found by using the Mach angle corresponding to the previous Prandtl-Meyer function. Note that the position at C also changes, so the iteration procedure for position C must be conducted.

This procedure is repeated until $(\nu_{III})_m - (\nu_{III})_{(m-1)} < \varepsilon$. Equation (B-1) is solved.

Now, if both conditions are satisfied (oblique shock equations-rotational flow characteristics net), $\nu_{B.S.} - \nu_{M.C.} < \varepsilon$. If not, θ_2 is incremented by a small value, $\Delta\theta_2$, with the attendant iterations until this condition is met.

Rotational Characteristic - Tube Wall Intersection

The conditions at D on the wall must be satisfied so that the solution may progress along the wall for points past B. This is done by solving the finite difference equations for the characteristics extending from point III to D.

$$[\nu]_D - [\nu - \theta]_{III} = \frac{1}{\cot\left[\frac{\mu_D + \mu_{III}}{2}\right] + \cot\frac{\theta_{III}}{2}} \; \frac{\left[r_t - r_{III}\right]}{\frac{1}{2}\left[r_t + r_{III}\right]}$$

$$+ \frac{\sin\left[\mu_{III} + \mu_D\right]}{2\,\gamma} \; \frac{\left[\frac{P_{0_I}}{P_0} - \frac{P_{0_{III}}}{P_0}\right]}{\frac{1}{2}\left[\frac{P_{0_I}}{P_0} + \frac{P_{0_{III}}}{P_0}\right]} \qquad \text{(B-3)}$$

$$\frac{r_t - r_{III}}{z_D - z_{III}} = \tan\left[\frac{\theta_{III}}{2} + \frac{\mu_{III} + \mu_D}{2}\right] \quad . \qquad \text{(B-4)}$$

To solve these equations, ν_D must be known. In this case, assume for the first estimate $\nu_D = \nu_B$ and iterate until

$$\left[\nu_{D(m-1)} - \nu_{D(m)}\right] < \epsilon \quad .$$

An equation must be used to describe the variation of Mach number along the wall as a function of z.

Suppose the z position of C is known, but ν_C is unknown. Remember the flow conditions and positions of A and B are known. Now, if A and B are sufficiently close, ν_C may be obtained by

$$\nu_C = \nu_A + \left(\frac{\Delta\nu}{\Delta z}\right)_A \Delta z$$

$$\nu_C = \nu_A + \frac{\nu_B - \nu_A}{z_B - z_A}\left(z_C - z_A\right) \quad . \qquad \text{(B-5)}$$

Initial Rotational Characteristic - Shock Wave Intersection

In the solution for point III behind the shock and D on the wall, the flow conditions along the wall were known out to B along the wall. However, in solving for point II, only the conditions behind the shock at point I and the wall streamline are known.

This problem is solved numerically by letting the conditions behind the shock at I equal to the conditions at A (first approximation) and solving for the conditions behind the shock. We then project to the wall at B through Equations (B-4) and (B-5). Now Equation (B-5) is solved to obtain a better estimate of ν_A. This process is repeated until

$$\left[\nu_{A(m-1)} - \nu_{A(m)}\right] < \epsilon \quad .$$

Accuracy Discussion

The primary purpose of this exercise is to determine the pressure along the wall aft of the impingement shock. Prior to this time, approximate methods, such as Bauer [17] simplified theory, assumed that the flow behind the shock was two-dimensional, was deflected parallel to the wall, and that the pressures behind the shock were impressed on the wall. He bases the justification for this simplified theory on the premise that the variation of the flow angle with respect to that assumed is small, i.e., $\theta_2 = \delta$, and that he has neglected second-order terms δ^2. Bauer also limits the applicability of this theory to the region near the shock.

A complete computer program which would define the flow via the method of characteristics for multiple shock flows was initiated by Kuo [27]. However, Kuo was unable to complete this formidable task because of a lack of funding. A more exact technique is well within the state-of-the-art of computer science, provided one has the time and funds.

The parameter in the equation which differentiates axisymmetric flow from two-dimensional plane flow is

$$\frac{1}{\cot \mu \pm \cot \theta} \frac{dr}{r} .$$

Note as the flow angle, θ, approaches zero, the cot θ approaches infinity, and if the other terms remain finite, the overall term tends toward zero. Now, if the point under consideration is near the wall, dr or Δr is small and r is large, and θ is small, this term can be neglected and the flow reverts to two-dimensional plane flow as was Bauer's assumption. However, in our case, θ is small but maybe not that small, and dr or Δr can be large, depending on the distance of the point under consideration from the wall streamline. The question is how large can the relation $\frac{\Delta r}{r}$ be, or how close to the tube axis will the calculation yield acceptable answers. Certainly the acceptability depends on θ which is not known. Another problem exists, considering that ΔP_0 may not be small even if Δr is. If ΔP_0 is large, then acceptable results are obtained only if the entropy term can be integrated, i.e.,

$$\int_1^2 \frac{\sin 2\,\mu}{2\,\gamma}\,\frac{dP_0}{P_0} \quad .$$

To do this, sin 2 μ must be a constant or not a function of P_0. This, in a way, is a contradiction, because in the axisymmetric term, θ appears with μ. So, if μ tends toward a constant, then this term cannot be integrated, which is required if Δr is large. However, if in reality μ is small and μ does not vary too strongly along a characteristic, this term will tend toward a constant and reasonable estimates for large values of Δt and ΔP_0 may be obtained. Because a shock tends to process a nonuniform flow field toward these requirements, the prospect seems good that reasonable estimates will be obtained. However, in reality, a comparison of the analytical estimates to experimental values seems to be the best method of determining an accuracy limitation which would answer the basic question.

APPENDIX C

FLOW CHARACTERISTICS

Table C-I. Cold Flow Isentropic Characteristics $\frac{P_b}{P_0} = 0.0244$, $\gamma = 1.4$

(For Characteristics Net in Figure C-1)

Points	Mach No.	Flow Angle (deg)	$\frac{P}{P_0}$	Points	Mach No.	Flow Angle (deg)	$\frac{P}{P_0}$
00	2.777	20.000	0.03815	22	3.031	21.971	0.02598
01	2.848	21.470	0.03420	23	3.114	23.454	0.02297
02	2.921	22.940	0.03066	24	3.199	24.936	0.02024
03	2.996	24.410	0.02739	25	3.132	23.156	0.02237
04*	3.073	25.880	0.02440	26*	3.073	21.527	0.02440
10	2.825	19.500	0.03545	30	2.924	18.500	0.03052
11	2.899	20.978	0.03168	31	3.005	19.997	0.02703
12	2.976	22.455	0.02824	32	3.088	21.488	0.02386
13	3.054	23.931	0.02510	33	3.175	22.978	0.02099
14	3.136	25.407	0.02224	34	3.265	24.465	0.01839
15*	3.073	23.641	0.02440	35	3.192	22.672	0.02047
20	2.874	19.000	0.03291	36	3.129	21.031	0.02247
21	2.951	20.487	0.02928	37*	3.073	19.519	0.02440

* Jet Boundary

PRECEDING PAGE BLANK-NOT FILMED

Table C-I. Continued

Points	Mach No.	Flow Angle (deg)	$\frac{P}{P_0}$	Points	Mach No.	Flow Angle (deg)	$\frac{P}{P_0}$
40	2.975	18.000	0.02827	60	3.079	17.000	0.02418
41	3.059	19.507	0.02492	61	3.172	18.530	0.02109
42	3.147	21.006	0.02189	62	3.267	20.043	0.01833
43	3.114	22.502	0.01914	63	3.368	21.554	0.01584
44	3.332	23.996	0.01667	64	3.473	23.060	0.01363
45	3.253	22.189	0.01871	65	3.381	21.225	0.01554
46	3.185	20.535	0.02067	66	3.303	19.544	0.01741
47	3.126	19.013	0.02256	67**	3.254	18.437	0.01868
				70	3.133	16.500	0.02231
Jet Boundary-Wall Intersection**	3.073	18.197	0.02440	71	3.230	18.049	0.01935
48	3.096	18.216	0.02359	72	3.330	19.563	0.01673
50	3.027	17.500	0.02616	73	3.435	21.082	0.01438
51	3.115	19.018	0.02294	74	3.546	22.594	0.01229
52	3.206	20.524	0.02004	75	3.447	20.744	0.01414
53	3.302	22.028	0.01743	76	3.363	19.049	0.01594
54	3.402	23.528	0.01509	77**	3.351	18.792	0.01622
55	3.316	21.707	0.01707	80	3.189	16.000	0.02057
56	3.243	20.039	0.01898	81	3.289	17.552	0.01775
57	3.180	18.507	0.02083	82	3.394	19.084	0.01525
58**	3.171	18.268	0.02112	83	3.505	20.610	0.01302

** Shock Intersection

Table C-I. Concluded

Points	Mach No.	Flow Angle (deg)	$\frac{P}{P_0}$	Points	Mach No.	Flow Angle (deg)	$\frac{P}{P_0}$
84	3.621	22.128	0.01105	110	3.361	14.500	0.01599
85	3.515	20.263	0.01283	111	3.476	16.084	0.01356
86**	3.480	19.600	0.01349	112	3.598	17.651	0.01142
				113**	3.628	18.022	0.01095
90	3.245	15.500	0.01894				
91	3.350	17.062	0.01625	120	3.422	14.000	0.01466
92	3.460	18.606	0.01387	121	3.542	15.597	0.01235
93	3.576	20.140	0.01177	122**	3.610	16.443	0.01123
94**	3.696	21.632	0.00995				
				130	3.483	13.500	0.01343
100	3.303	15.000	0.01741	131**	3.600	14.995	0.01138
101	3.413	16.573	0.01485				
				140	3.546	13.000	0.01228
102	3.528	18.128	0.01260				
				141**	3.595	13.607	0.01146
103	3.650	19.670	0.01062				
104**	3.656	19.743	0.01053	150**	3.604	12.500	0.01132

** Shock Intersection

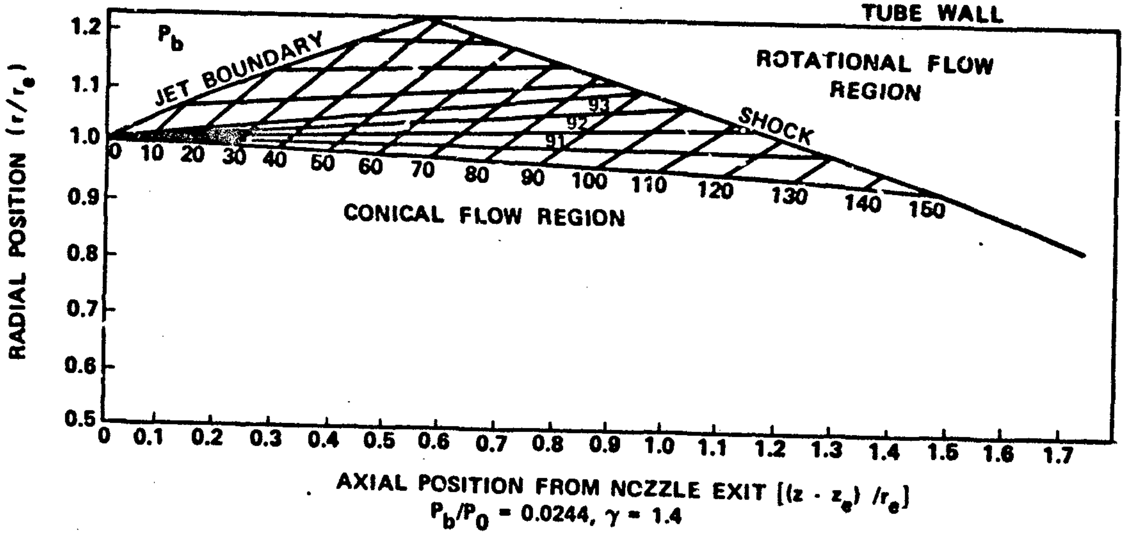

Figure C-1. Isentropic Characteristics

Net for Cold Flow $\frac{P_b}{P_0} = 0.0244,\ \gamma = 1.4$

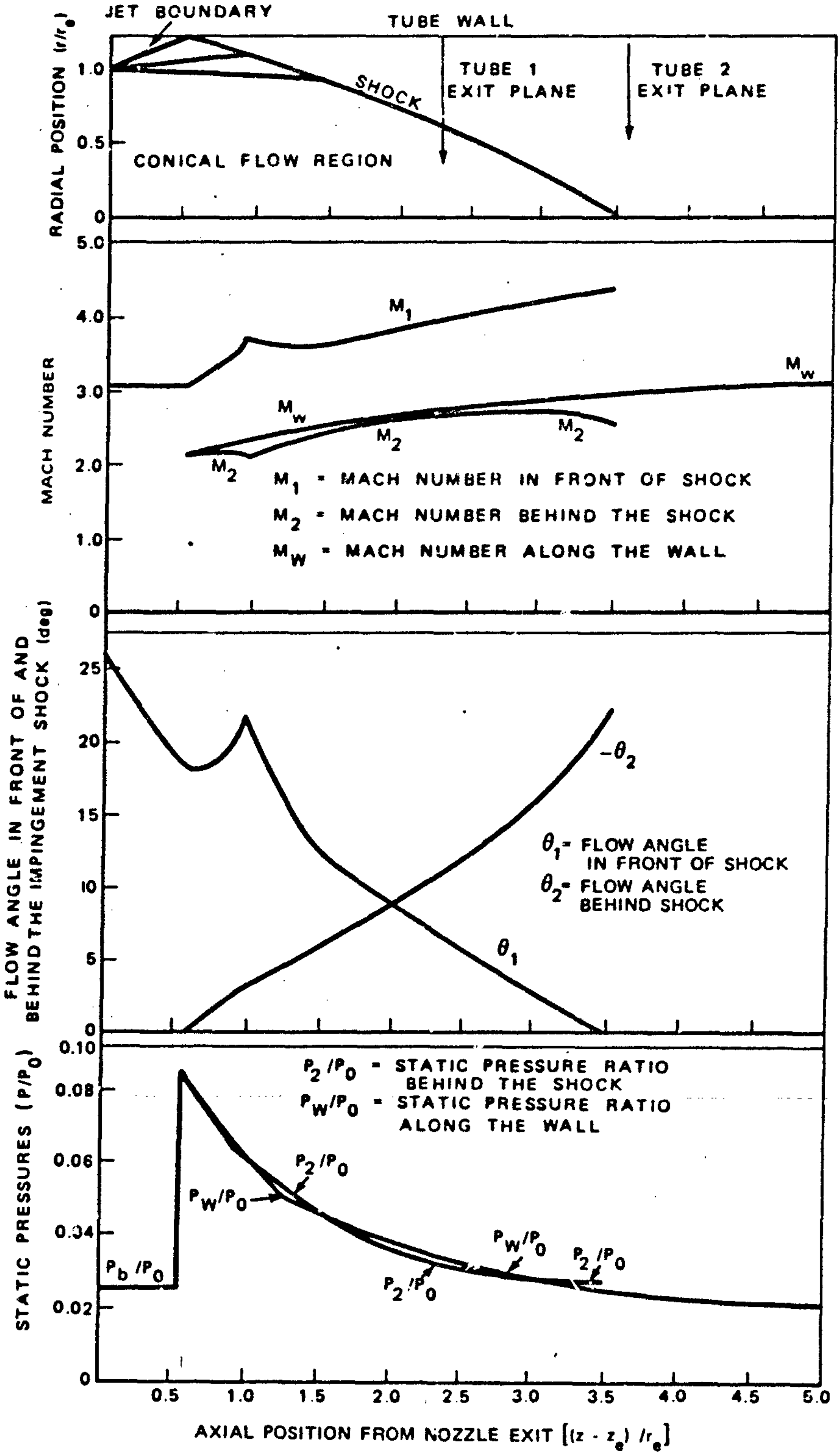

Figure C-1. Concluded

Table C-II. Hot Flow Isentropic Characteristics $\frac{P_b}{P_0} = 0.0118$, $\gamma = 1.2$

(For Characteristics Net in Figure C-2)

Points	Mach No.	Flow Angle (deg)	$\frac{P}{P_0}$	Points	Mach No.	Flow Angle (deg)	$\frac{P}{P_0}$
00	2.941	20.000	0.02493	30	3.053	18.500	0.0203
01	3.039	22.627	0.02084	31	3.164	21.183	0.0166
02	3.141	25.254	0.01734	32	3.278	23.859	0.0135
03	3.246	27.880	0.01434	33	3.398	26.530	0.0109
04*	3.354	30.507	0.01180	34	3.524	29.194	0.0087
				35	3.457	27.064	0.0098
10	2.978	19.500	0.02330	36	3.402	25.168	0.0108
11	3.080	22.144	0.01935	37**	3.354	24.219	0.0118
12	3.186	24.787	0.01598				
13	3.296	27.429	0.01311	40	3.092	18.000	0.01895
14	3.410	30.068	0.01068	41	3.206	20.703	0.01541
15*	3.354	27.981	0.01180	42	3.326	23.396	0.01242
				43	3.451	26.081	0.00992
20	3.015	19.000	0.02177	44	3.583	28.757	0.00784
21	3.122	21.664	0.01796	45	3.510	26.607	0.00892
22	3.232	24.323	0.01471	46**	3.451	24.711	0.00992
23	3.347	26.979	0.01196				
24	3.466	29.631	0.00964	50	3.131	17.500	0.01766
25	3.405	27.523	0.01129	51	3.249	20.224	0.01425
26*	3.354	25.644	0.01180	52	3.374	22.935	0.01139

* Jet Boundary
** Shock Intersection

Table C-II. Concluded

Points	Mach No.	Flow Angle (deg)	$\frac{P}{P_0}$	Points	Mach No.	Flow Angle (deg)	$\frac{P}{P_0}$
53	3.504	24.634	0.00901	90	3.291	15.500	0.01321
54	3.643	28.320	0.00705	91	3.428	18.314	0.01033
55	3.564	26.150	0.00810	92	3.573	21.097	0.00797
56*	3.540	25.437	0.00846	93**	3.594	21.474	0.00768
60	3.170	17.000	0.01644	100	3.333	15.000	0.01226
61	3.293	19.745	0.01317	101	3.475	17.839	0.00951
62	3.422	22.474	0.01044	102**	3.569	19.611	0.00803
63	3.559	24.187	0.00818				
				110	3.375	14.500	0.01137
64	3.704	27.884	0.00633				
				111	3.522	17.364	0.00874
65**	3.663	26.069	0.00679				
				112**	3.554	17.956	0.00825
70	3.210	16.500	0.01530				
71	3.337	19.267	0.01216	120	3.417	14.000	0.01054
72	3.472	22.014	0.00955	121**	3.545	16.434	0.00838
73	3.614	24.742	0.00741				
				130	3.460	13.500	0.00975
74**	3.677	25.873	0.00663				
				131**	3.539	14.977	0.00847
80	3.250	16.000	0.01422				
				140	3.504	13.000	0.00902
81	3.38[illegible]	18.790	0.01121				
				141**	3.540	13.655	0.00847
82	3.522	21.555	0.00873				
83**	3.628	23.521	0.00723	150**	3.546	12.500	0.00836

* Jet Boundary
** Shock Intersection

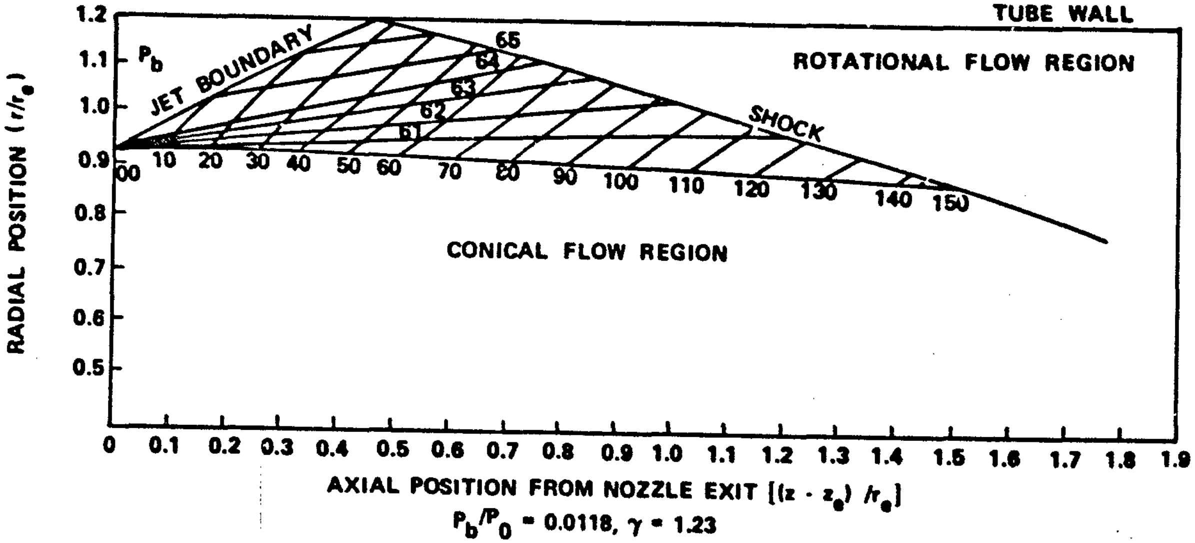

Figure C-2. Isentropic Characteristics

Net for Hot Flow $\frac{P_b}{P_0} = 0.0118$, $\gamma = 1.23$

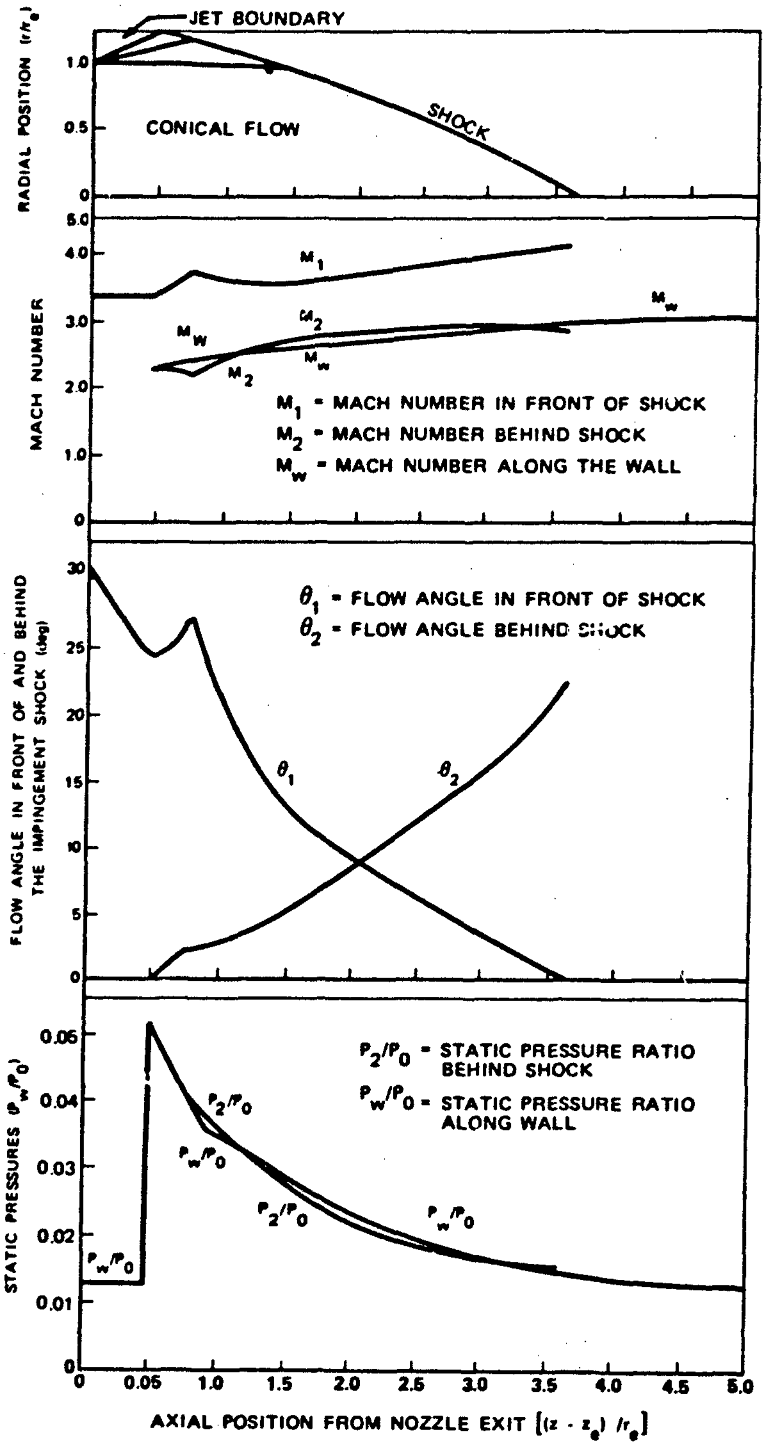

Figure C-2. Concluded

LIST OF REFERENCES

1. Nusselt, W., "Der Druck im Ringquerschnitt von Rohren mit plotzlicher Erweiterung beim Durchfluss von Luft mit hoher geschwindigkeit," Ver. deut. Ing. Berlin Forschung., 11 Bd., Heft 5, September 1940, 250-255.

2. Wick, R. S., "The Effect of Boundary Layer on Sonic Flow Through an Abrupt Cross-Sectional Area Change," J. Aeronaut. Sci., 20, October 1953, 675-682.

3. Fabri, J., and Siestrunck, R., "Etude des divers regimes d'e coulement dans L'e Largissement brusque d'une veine supersonique," Rev. Generale des Sciences Appliquees, 2, 1955, 229-237.

4. Fabri, J., and Siestrunck, R., "Supersonic Air Ejectors," Adv Appl Mech, V, Academic Press, Inc., New York, 1958, 1-34.

5. Crocco, L., "One-Dimensional Steady Gas Dynamics," Fundamentals of Gas Dynamics, ist Ed., III, Princeton University Press, New Jersey, 1958, 287-293.

6. Hermann, R., "Diffuser Efficiency of Free-Jet Supersonic Wind Tunnels at Variable Test Chamber Pressure," J. Aeronaut. Sci., 19, June 1952, 375-384.

7. Fabri, J., and Paulon, J., "Theory and Experiments on Super-Sonic Air-to-Air Ejectors," NACA TM-1410, September 1958.

8. Goethert, B. H., "Some Selected Problems in Engine Altitude Testing," AEDC-TR-58-15, October 1958.

9. Taylor, D., "A Summary of Full-Scale Rocket Exhaust Gas Diffuser Performance in the Engine Test Facility," AEDC-TM-59-13, July 1959.

10. Barton, D. L., and Taylor, D., "An Investigation of Ejectors Without Induced Flow," AEDC-TN-59-145, December 1959.

11. Foster, R. M., "The Supersonic Diffuser and Its Application to Altitude Testing of Captive Rocket Engines," AFFTC-TR-60-1, January 1960.

12. Goethert, B. H., and Taylor, D., "High Altitude Testing of Propulsion Systems," Z. Flugwiss, 8, Heft 7, 1960, 202-211.

PRECEDING PAGE BLANK-NOT FILMED

13. Mickola, R. H., "Performance Summary of the Supersonic Diffuser and its Application to Altitude Testing of Captive Rocket Engines," Addendum 1 to AFFTC-TR-60-1, April 1961.

14. Bauer, R. C., and German, R. C., "Some Reynolds Number Effects on the Performance of Ejectors Without Induced Flow," AEDC-TN-61-87, August 1961.

15. German, R. C., and Bauer, R. C., "Effects of Diffuser Length on the Performance of Ejectors Without Induced Flow," AEDC-TN-61-89, August 1961.

16. Bauer, R. C., "Characteristics of Axisymmetric and Two-Dimensional Isoenergetic Jet Mixing Zones," AEDC-TDR-63-253, December 1963.

17. Bauer, R. C., "Theoretical Base Pressure Analysis of Axisymmetric Ejectors Without Induced Flow," AEDC-TDR-64-3, January 1964.

18. German, R. C., Bauer, R. C., and Panesci, J. H., "Methods for Determining the Performance of Ejector-Diffuser Systems," J. Spacecraft, 3, No. 2, February 1966, 193-200.

19. Korst, H. H., Chow, W. L., and Sumwalt, G. W., "Research on Transonic and Supersonic Flow of a Real Fluis at Abrupt Increases in Cross Section," University of Illinois, ME Technical Report 392-5, December 1959.

20. Crocco, L., and Lees, L., "A Mixing Theory in the Interaction Between Dissipated Flows and Nearly Isentropic Streams," J. Aeronaut. Sci., 19, No. 10, October 1952, 649-676.

21. Greenwood, T. F., "An Analytical Study of the Base Flow Problem Including the Theories of Korst, Zumwalt, and Nash," Brown Engineering Company, Inc., Tech. Memo. AA-3-65-8, March 1965.

22. Greenwood, T. F., "An Integral Model for the Turbulent Supersonic Near Wake Employing Strong Interaction Concepts," University of Texas, Ph.D. Dissertation, 1971.

23. Lamb, J. P., and Hood, C. G., "An Integral Analysis of Turbulent Reattachment Applied to Plane Supersonic Base Flows," Trans. of ASME, 90, Series B, 1968, 553-560.

24. Owczarek, J. A., "Spatial Supersonic Flows," Fundamentals of Gas Dynamics, 1st ed., International Text Book Co., Pennsylvania, 1964, 472-481.

25. Gracey, W. A., "Wind-Tunnel Investigation of a Number of total-Pressure Tubes at High Angles of Attack," NACA Report 1303, 1957.

26. Ferri, A., "The Method of Characteristics," General Theory of High Speed Aerodynamics, 1st ed., VI, Princeton University Press, New Jersey, 1954, 616-635.

27. Ruo, S. Y., "Development of a Multiple Shock Computer Program Using a Streamline-Normal Technique," HREC-0186-1. Lockheed Missile and Space Company, January 1968.

28. Ferri, A., "Supersonic Flows with Shock Waves," General Theory of High Speed Aero-Dynamics, 1st ed., VI, Princeton University Press, New Jersey, 1954, 670-690.

29. Moe, M. M., "The Computation of Jet Flows with Shocks," Space Technology Laboratories, Inc., TR-59-0000-0061, May 1959.

30. Ihrig, H. K., and Korst, H. H., "Quasi-Steady Aspects of the Adjustment of Separated Flow Regions to Transient External Flows," AIAA Journal, 1, No. 4, April 1963, 934-936.

31. Addy, A. L., "Detailed Analyses for the Base-Pressure Programs TSABPP-1, 2," U. S. Army Missile Command, Report No. RD-TN-69-7, August 1969.

32. Personal Communication with Dr. B. J. Walker, Aeroballistics Directorate, DRDE&MSL, U. S. Army Missile Command.